A fully autonomous ozone, aerosol and night time water vapor LIDAR: a synergistic approach to profiling the atmosphere in the Canadian oil sands region

Kevin B. Strawbridge[1], Michael S. Travis[1], Bernard J. Firanski[1], Jeffrey R. Brook[1], Ralf Staebler[1] and Thierry Leblanc[2]

[1]{Air Quality Processes Research Section, Environment and Climate Change Canada, Toronto, ON, Canada}

[2]{ California Institute of Technology, Jet Propulsion Laboratory, Wrightwood, CA 92397, USA.}

Correspondence to: Kevin B. Strawbridge (Kevin.Strawbridge@canada.ca)

Abstract

LIDAR technology has been rapidly advancing over the past several decades. It can be used to measure a variety of atmospheric constituents at very high temporal and spatial resolutions. While the number of LIDARs continues to increase worldwide, there is generally a dependency on an operator, particularly for high-powered LIDAR systems. Environment and Climate Change Canada (ECCC) has recently developed a fully autonomous, mobile LIDAR system called AMOLITE (Autonomous Mobile Ozone LIDAR Instrument for Tropospheric Experiments) to simultaneously measure the vertical profile of tropospheric ozone, aerosol and water vapor (night time only) from near ground to altitudes reaching ten to fifteen kilometers. This current system uses a dual laser, dual LIDAR design housed in a single climate-controlled trailer. Ozone profiles are measured by the DIfferential Absorption LIDAR (DIAL) technique using a single 1 m Raman cell filled with CO_2. The DIAL wavelengths of 287 nm and 299 nm are generated as the second and third Stokes lines resulting from stimulated Raman scattering of the cell pumped using the fourth harmonic of a Nd:YAG laser (266nm). The aerosol LIDAR transmits three wavelengths simultaneously (355 nm, 532 nm and 1064 nm) employing a detector designed to measure the three backscatter channels, two nitrogen Raman channels (387 nm and 607 nm), and one cross-polarization channel at 355 nm. In addition, we ~~have~~ added a water vapor channel arising from the Raman-shifted 355nm output (407nm) to provide nighttime water vapor profiles. AMOLITE participated in a validation experiment alongside

four other ozone DIAL systems before being deployed to the ECCC Oski-ôtin ground site in the Alberta Oil Sands region in November 2016. Ozone was found to increase throughout the troposphere by as much as a factor of 2 from stratospheric intrusions. The dry stratospheric air within the intrusion was measured to be less than 0.2 g/kg. A biomass burning event that impacted the region over an eight-day period produced LIDAR ratios of 35 to 65 sr at 355 nm and 40 to 100 sr at 532. Over the same period the Angstrom exponent decreased from 1.56 ± 0.2 to 1.35 ± 0.2 between the 2 to 4 km smoke region. ~~The advantage of nearly continuous measurements obtained over a 12-month period will be presented, highlighting the synergistic advantage of AMOLITE's tri-LIDAR design.~~

1 Introduction

Tropospheric ozone, aerosols and water vapor are important atmospheric constituents affecting air quality and climate. Ozone is a short-lived climate pollutant (SLCP) and air pollutant that can have detrimental impacts on human health (Malley et al., 2015, Lippmann, 1991), agriculture (McKee, 1994) and ecosystems (Ashmore, 2005) when present at high enough concentrations. Tropospheric ozone is photo-chemically produced primarily from nitrogen oxides and volatile organic compounds (VOCs) from anthropogenic sources, biogenically produced from forest fires (Aggarwal et al., 2017 and Trickl et al., 2015) and can be enhanced through stratospheric/tropospheric transport (STT) events (Ancellet et al., 1991, Langford et al., 1996, Leblanc et al., 2011 and Stohl~~Trickl~~ et al., 1999~~2014~~). Both of these latter sources can have significant impacts on ozone concentration although typically their impacts vary within the vertical distribution of the troposphere. The advantage of ozone DIAL is the ability to measure this vertical column with high enough temporal resolution to understand atmospheric mixing and exchange processes. Along with ozone, the vertical distribution of aerosols and water vapor can also vary considerably throughout the troposphere.

Aerosols or particulate matter are tiny particles suspended in the air which contribute to the radiative budget, are a tracer for pollution transport and impact visibility, cloud formation and air quality. They affect the earth's climate by interacting with the sun and earth's radiation (Ramanathan, 2001) and by modifying clouds (Feingold et al., 2003 and Twomey, 1977) and depending on their size and the meteorological conditions can travel over great distances around the globe (Uno et al., 2009). In high enough concentrations these particles can have dramatic effects on visibility (Li et al., 2016 and Singh, 2017) and cause respiratory problems, particularly in those suffering from lung conditions such as asthma. This has been the motivation for several countries to adopt an air quality index (Kousha et al., 2015) to alert the public to respiratory dangers during pollution events. Aerosol backscatter LIDAR systems are uniquely capable of providing the vertical profile of tropospheric aerosols at very high temporal and spatial resolutions and are therefore, ideal instruments to study the transport and optical properties of aerosol~~s processes outlined above~~. While the vertical distribution of ozone and aerosols can be highly variable throughout the troposphere, water vapor tends to have the highest concentration closest to the surface and throughout the mixed layer.

Water vapor plays a pivotal role in climate change and atmospheric stability by directly influencing many atmospheric processes such as cloud formation (Pruppacher and Klett, 1997)

and photochemical atmospheric reactions (Yamamoto et al., 1966 and Grant, 1991). Furthermore, tropospheric water vapor is a catalyst to many atmospheric chemical reactions by functioning as a solvent for chemical products of natural and anthropogenic activities (Grant, 1991). Also, as ~~one of~~ the primary greenhouse gas~~es~~, with strong infrared absorption in the 100-600 cm^{-1} spectral region, water vapor helps to maintain the earth's radiation balance by absorbing and emitting infrared radiation (Twomey, 1991, Clough et al., 1992 and Sinha and Harries, 1995). The high spatial and temporal variability of water vapor throughout the atmosphere makes it an ideal candidate for LIDAR measurements (Vogelmann et al., 2015).

The purpose of this paper is to describe a vertical profile measurement system that measures ozone, aerosols and water vapor simultaneously. By employing three different LIDAR techniques - Mie backscatter LIDAR, water vapor Raman LIDAR and ozone DIAL - in one observation platform we are able to explore a synergistic approach to advance our understanding of the trace gas distribution in the lower atmospher~~eic dynamics~~ with the eventual goal of supporting development to improve air quality forecasts, diagnostic models and satellite measurements. There are only a few sites that currently exist where all three LIDAR techniques are operated: Garmisch-Partenkirchen ~~Zugspitze~~ (Trickl et al., 2015), Maïdo observatory Reunion Island (Baray et al., 2013) and Observatoire de Haute-Provence (OHP) (Bock et al., 2013, Khaykin et al., 2017 and Gaudel et al., 2015). Several ~~However, all~~ of these sites are high altitude sites that began as stratospheric observatories.

The accomplishment here was to develop such a platform to be mobile and to run autonomously providing near continuous observations (except during precipitation events), even in remote areas. Environment and Climate Change Canada (ECCC) has designed and built a fully autonomous, mobile LIDAR system, based on the backbone of an earlier system design (Strawbridge, 2013), named AMOLITE (Autonomous Mobile Ozone LIDAR Instrument for Tropospheric Experiments) to ~~simultaneously~~ measure the vertical profile of tropospheric ozone, aerosol and water vapor simultaneously. To verify the system's performance AMOLITE participated in a validation campaign known as the Southern California Ozone Observation Project (SCOOP) at the Jet Propulsion Laboratory's Table Mountain Facility in Wrightwood, CA during August, 2016. This study brought together five of the six tropospheric ozone LIDARs that form the Tropospheric Ozone LIDAR Network – TOLNet (- http://www-air.larc.nasa.gov/ missions/TOLNet/). In addition to the five LIDARs, ozone sonde balloons were launched throughout the study period. This campaign provided an excellent opportunity

to evaluate the ozone profiles produced by AMOLITE. For details of the inter-comparison refer to a separate publication (manuscript in preparation). LIDAR networks (ndacc-lidar.org, mplnet.gsfc.nasa.gov, Papayannis et al., 2008 and Sugimoto et al., 2009) are very important scientific tools that allow the collective benefit of increased geographical coverage (Langford et al., 2018 and Trickl et al., 2016) and can often provide valuable climatological data (Granados-Munoz et al., 2016, Khaykin et al., 2017 and Gaudel et al., 2015). The existence of networks like TOLNet will help to address the need for more ozone profilers in the troposphere as reported ~~It has also been shown~~ in the recent Tropospheric Ozone Assessment Report (TOAR) by Gaudel et al., (2018). ~~the lack of ozone profilers in the troposphere to further support the existence of networks like TOLNet.~~

After the validation campaign, AMOLITE was shipped back to Canada where it was made ready for deployment to the oil sands region. The first AMOLITE ~~first light~~ ozone and water vapor profiles ~~were acquired on 3 November 2016~~ at the Oski-ôtin ground site in Fort McKay, Alberta, were acquired on 3 November 2016~~B~~. In addition to the LIDAR measurements, operation of a windRASS (wind radio-acoustic sounding system – model MFAS, Scintec, Rottenburg, Germany) provides the local meteorological wind fields at 10m vertical resolution from 40 m to typically 500m above ground, directly determining the upwind sources near ground level and aloft over the site. These remote sensors provide a coherent 3D picture of the transport processes impacting the ground site and the region nearby. Also housed in a trailer on site is a chemistry observing platform ~~facility~~ called CAM1 ~~(good reference here for CAM1)~~ that has an extensive suite of ground-based instrumentation that continuously measures a variety of gaseous and particulate pollutants. The purpose of this site is to identify the predominant sources impacting the region and the main local-scale atmospheric processes influencing pollutant transport, transformation and deposition. This information will be used to improve our knowledge of what is being emitted and the processes in the atmosphere that affect where the pollutants move and deposit.

The focus of this paper will be on the additional development required to add the ozone and water vapor capability to the previous autonomous aerosol LIDAR design developed by ECCC, followed by a brief section on the validation and verification of the instrument and processing algorithms. The fourth section will describe a few case studies acquired throughout the first year of operation at the Oski-ôtin ground site in Fort McKay. The final section will draw conclusions and discuss some future improvements that are currently underway for AMOLITE.

2 LIDAR technique

The AMOLITE instrument uses~~In this paper we are using~~ three different LIDAR techniques to measure different atmospheric constituents: a Mie backscatter LIDAR to measure the vertical profile of aerosol at three different wavelengths, a DIfferential Absorption LIDAR (DIAL) to measure the vertical ozone profile and a Raman LIDAR to measure the water vapor profile. The Mie backscatter aerosol lidar technique used~~employed~~ in AMOLITE, has already been described in detail by Strawbridge, 2013. Here we briefly describe the DIAL and Raman LIDAR techniques used for the systems in AMOLITE.

2.1 Ozone DIAL Technique

Using the DIAL technique, it is possible to retrieve ozone mixing ratios from the backscatter profiles. The technique essentially uses the differential absorption of ozone at two different wavelengths that are relatively close together to minimize aerosol effects, but far enough apart to have a sufficiently large difference in their ozone absorption cross sections. Consequently, the ozone calculation uses the two-wavelength solution of the lidar equation given below (Kovalev et al., 1994):

$$N(z) = \frac{-1}{2(\alpha_{on}-\alpha_{off})}\left[\frac{d}{dz}\left[ln\frac{P_{on}(z)}{P_{off}(z)} - ln\frac{\beta B_{on}(z)}{\beta B_{off}(z)}\right] + 2\Delta\sigma(z) + 2\sum_i \Delta\alpha_i n_i(z)\right] \quad (1)$$

~~(1)~~

where

$\alpha_{on} - \alpha_{off}$ is the differential ozone absorption cross section, $\frac{P_{on}(z)}{P_{off}(z)}$ is the signal ratio, $\frac{\beta B_{on}(z)}{\beta B_{off}(z)}$ is the ratio of the backscatter coefficient at the "on" and "off" wavelengths~~ratio~~ and $2\Delta\sigma(z)$ is the total two-way ~~scatter or~~ extinction coefficient differential, $\Delta\alpha_i$ is the differential cross section of the interfering trace gas and $n_i(z)$ is the number density profile of the interfering trace gas.~~.~~ In our system, ~~the signal at~~ 287 nm represent~~s~~ing the "on" wavelength~~signal~~ and 299 nm represent~~s~~ing the "off" wavelength~~signal~~. ~~Solving for the component of the backscatter due to the molecular contribution and the aerosol contribution, I~~it is possible to express the backscatter contribution overall to the ozone calculation at the on and off wavelengths based solely on the

ratio between the aerosol and molecular backscatter, $B^*(z)$, at some reference wavelength., ~~referred to by Kovalev as the backscatter ratio $S(z)$.~~ This is represented by

$$\frac{d}{dz}\left\{ln\left[\frac{\beta_{on}(z)}{\beta_{off}(z)}\right]\right\} = \frac{d}{dz}\left\{ln\left[\frac{1+B^*(z,\lambda_{ref})\left(\frac{\lambda_{on}}{\lambda_{ref}}\right)^{4-v}}{1+B^*(z,\lambda_{ref})\left(\frac{\lambda_{off}}{\lambda_{ref}}\right)^{4-v}}\right]\right\} \quad (2)$$

~~$$\frac{B_{on}(z)}{B_{off}(z)} = \frac{1+S(z,\lambda_{ref})\left(\frac{\lambda_{on}}{\lambda_{ref}}\right)^{4-v}}{1+S(z,\lambda_{ref})\left(\frac{\lambda_{off}}{\lambda_{ref}}\right)^{4-v}} \quad (2)$$~~

Where v is the Angstrom exponent representing the wavelength dependence of aerosol Mie backscatter and in our case the reference wavelength is 355 nm. The difficulty arises in determining the Angstrom exponent in regions where the aerosol concentrations are lower and with enough precision to provide an accurate correction. This point is illustrated for a forest fire case shown in Section 4.3.

~~In the case of AMOLITE a boxcar filter is used to produce a simple smoothing of the raw data followed by a second-order Savitzky-Golay convolution $\frac{\beta_{on}(z)}{\beta_{off}(z)}$. Although the Savitsky-Golay approach may cause issues at the top of the stratospheric ozone profiles (Godin et al., 1999) it does not have as much of a negative impact for tropospheric ozone due to the vertical structure of ozone typically increasing at the top of the profile. This is primarily due to the signal-to-noise ratio being large enough at most altitudes. Alternate, more sophisticated filters are being considered and may be implemented in future data versions, but for now all TOLNet LIDARs are using the same approach. Tropospheric ozone DIAL along with water vapour LIDAR can provide complimentary datasets when investigating transport or process studies.~~

2.2 Water Vapor Raman Technique

During the early stages of the optical detector design for the aerosol LIDAR, it was determined that with the addition of a few optics (see Figure 2), that requires very little additional space in the detector design, it would be possible to measure nighttime water vapor using the Raman technique on the 355 nm laser wavelength. This would be particularly valuable when identifying STT events where the dry stratospheric air can be easily identified by the water vapor LIDAR measurements ~~(Trickl et al., 2014)~~. Raman scattering is an inelastic quantum-mechanical scattering process, in which the wavelength of the incident radiation is shifted as a result of the interaction of the photons with target molecules. The Raman wavelength shift,

related to the exciting laser wavelength (λ_L), is proportional to the distinct ro-vibrational energy levels and provides a unique fingerprint for each molecule. The Raman scattering process can either involve energy absorption by the molecule, producing Stokes Raman scattered light with less energy (longer wavelength) or energy transferred to the molecule, producing anti-Stokes Raman scattered light with more energy (shorter wavelength). In the framework of perturbation theory, Raman scattering corresponds to the absorption and subsequent emission of a photon via an intermediate electronic state, which is based on the target molecule ro-vibrational states, producing either a longer (Stokes) or shorter (anti-Stokes) wavelength shift. Most atmospheric species are vibrationally active; resulting in a net Raman shift to longer wavelengths ($\lambda_r > \lambda_L$), which indicates that atmospheric target molecules gain energy from the radiation field. The most probable Raman shifts for N_2 and H_2O are at 2330.7 cm^{-1} and 3652.0 cm^{-1}, respectively (Whiteman et al., 1992). Theoretically, Raman wavelength (λ_r) is related to the Raman shift (κ in cm^{-1}) by

$$\frac{1}{\lambda_r} = \frac{1}{\lambda_L} - \kappa \quad (3)$$

The general lidar equation for Mie-Rayleigh elastic backscattering for a given incident laser wavelength (λ) is given by (Whiteman, 2003)

$$P(z,\lambda) = P_o \frac{c\tau}{2} \frac{A}{z^2} \eta * O(z) \beta(z,\lambda) \exp\left\{-2\int \alpha(z',\lambda) dz'\right\}, \quad (4)$$

where P_o is the average power of a single laser pulse, τ is temporal pulse length of the laser, A is the detector area, η is the overall system efficiency (optical transmission from emitter to receiver and detection efficiency). $O(z)$ is the geometry factor containing the overlap function of the laser beam with the receiver field-of-view, β is the backscatter coefficient, which is the parameter that determines the strength of the signal being received by the telescope and the exponential term represents the two-way transmission loss as the laser propagates through the atmosphere where $\alpha(z)$ is the volume extinction coefficient due to molecular and aerosol contributions (Wandinger, 2005). For inelastic scattering process, Equation (4) above can be modified into

$$P(z,\lambda_l,\lambda_r) = P_o(\lambda_l) \frac{k^*}{z^2} O(Z) \beta(Z,\lambda_l,\lambda_r) \exp\{-\int_0^z [\alpha_l(\lambda_l,z') + \alpha_r(\lambda_r,z')] dz'\}, \quad (5)$$

~~where k^* is the lidar calibration constant, and α_l and α_r refer to the extinction coefficients (m^{-1}) resulting from the incident and Raman wavelengths, respectively (Aspey, et al., 2006). When the Raman backscatter coefficient is expressed in terms of the scattering cross section ($d\sigma/d\omega$ in $m^2 \cdot molecule^{-2} \cdot sr^{-1}$) of water vapor and nitrogen molecules and multiplied by the molecular number density $N(z)$ as (Aspey et al., 2006 and Ansmann, 1990) one gets~~

~~$$\beta(z,\lambda_l,\lambda_r) = N_r(z)\frac{d\sigma(\lambda_l,\lambda_r)}{d\Omega} \quad (6)$$~~

~~Substituting Eq.(6) into Eq. (5), and taking t~~The ratio between the water vapor and nitrogen Raman signals, yields a mathematical expression for the dependence of Raman signals ratio on water vapor and nitrogen molecular density (N_{H2O} and N_{N2}),~~-~~ namely

$$\frac{P(z,\lambda_l,\lambda_{H_2O})}{P(z,\lambda_l,\lambda_{N_2})} \propto R\frac{N_{H_2O}}{N_{N_2}}\frac{\left[d\sigma_{H_2O}/d\Omega\right]}{\left[d\sigma_{N_2}/d\Omega\right]}\exp\left\{-\int_0^z\left[\alpha(\lambda_{H_2O},z')-\alpha(\lambda_{N_2},z')\right]dz'\right\}_{11}^{10} \quad (3)$$

where R is the proportionality constant dependent on the instrument specifications. This equation ignores the temperature-dependent functions required for very narrow bandwidth filters, typically used for daytime operation (see Whiteman, 2003).

The water vapor mixing ratio (WVMR denoted as ($w(z)$) in grams of water vapor per kilogram of dry air) as a function of vertical altitude (z) is proportional to the ratio of the number density of water vapor to nitrogen, and is given by (Goldsmith et al., 1998):

$$w(z) = \frac{MW_{H_2O}}{MW_{DryAir}}\frac{N_{H_2O}(z)}{N_{DryAir}(z)} \approx \frac{MW_{H_2O}}{MW_{DryAir}}\frac{N_{H_2O}(z)}{N_{N_2}(z)/0.78} \approx 0.485\frac{N_{H_2O}(z)}{N_{N_2}(z)} \quad (4)$$

The WVMR equation above can be related to experimentally recorded Raman lidar signals, SG, by comparing equations~~Eqs~~. (3) and (4), leading to the following expression,

$$w(z) = D\frac{SG_{H_2O}}{SG_{N_2}} \quad (5)$$

where D (in g/kg) is a constant depending on instrumental specifications, ratio between N_2 and H_2O backscattering cross sections, N_2 mixing ratio, and Raman lidar signals extinction due to the aerosols and air molecules (Dionisi et al., 2009). The D constant is commonly evaluated by comparison with independent measurement (radiosonde) of water vapor mixing ratio ($w(z)$).

3 AMOLITE system design

3.1 Trailer Design and Infrastructure

The current system described here builds upon the successes of the autonomous aerosol LIDARS built over the past decade by ECCC (Strawbridge, 2013). AMOLITE uses a synergistic approach which combines a dual laser (for redundancy), dual LIDAR design (tropospheric ozone DIAL (DIfferential Absorption LIDAR and aerosol LIDAR) housed in the same trailer. In order to accommodate two LIDAR systems, the trailer needed to have a ~~be~~ slightly larger interior footprint of 2.1 m by 4.3 m feet long. A picture of AMOLITE, operating in full autonomous mode, deployed on a field experiment is shown in Figure 1a. The external infrastructure of the trailer was very similar to previous designs utilizing a meteorological tower, precipitation sensor enabled hatch cover, modified vertically-pointing radar interlock system and the other safety equipment required for operation of a class IV laser. The main differences in the design were the addition of a second radome to provide safety radar redundancy, larger hatch opening to allow the operation of two LIDAR receivers simultaneously and a greatly improved heating and cooling system. The second radar system allows one to remotely change between radar sources in the event that a system failure occurs. We found that these radomes would typically last between 2 and 4 years. However, when a failure occurs the LIDAR system is shut down for safety reasons until a site visit can be arranged and a new radar system installed. The addition of a second radar reduced system downtime and operational costs. The larger hatch not only is necessary for dual-LIDAR operation, but was also modified to allow the wiper system to operate while the hatch is either open or closed. It was also designed to accommodate exterior blower fans to prevent the accumulation of insects on the window attracted by the UV laser light. The most significant upgrade was the addition of two Mitsubishi Mr. Slim ducted units capable of delivering between 6000 and 24000 BTU of cooling ~~with external temperatures as low as -40C~~ as well as heat units mounted in the duct allowing an operational range of -40C to +40C. The ducting allows for better distribution of cool and warm air, maintaining a much more thermally stable environment throughout all the seasons of operation. The internal infrastructure of the trailer followed the early design of rack-mounted components and a single optical bench. The optical bench layout (see Figure 1b) was large enough to mount both LIDAR systems including the two laser sources per LIDAR. The details of the optical bench layout are discussed in Section 3.2 and 3.3. The main improvements ~~on the internal workings~~ of the trailer infrastructure were the inclusion of a battery-operated

propane furnace and charger capable of maintaining trailer heat for at least 48 hours in the event of a power failure. This is particular important should there be a power failure during the winter season, which can leave the trailer without heat for hours at a time causing the laser coolant to freeze, resulting in severe damage to the lasers. The other major change was the analog to digital computer card with a modular Advantech ADAM I/O system with greater flexibility and robustness. These improvements to the trailer infrastructure provided a more stable, reliable environment for improved data quality and uptime.

3.2 Aerosol LIDAR design

Since the aerosol LIDAR design described in Strawbridge, 2013 was the backbone of this new system only the changes will be discussed. The main differences are adding a laser for redundancy and adding an additional transmitted wavelength (355 nm) which in turn added the ability to acquire more particle information and a water vapor channel arising from the Raman shifted 355 nm output (407 nm) to provide night time water vapor profiles. The second identical laser, a Continuum Inlite III Nd:YAG operating at 20 Hz (see Figure 1b), shares the same steering mirror (see Figure 2) as the primary laser and can therefore be engaged remotely by a computer-controlled interface. The folding mirrors and steering mirror are ~~a~~ triple-coated (anti-reflection coating at 355 nm, 532 nm and 1064 nm) 50 by 6 mm flat with a high damage threshold, manufactured by Blue Ridge Optics,~~optic~~ mounted in a Thorlabs mount with encoded Thorlab actuators to permit remote alignment if necessary. A schematic of the aerosol LIDAR in Figure 2 shows the transmitter beam path and receiver design. The receiver was designed to image the aperture on the photomultiplier tube rather than the field stop. This is necessary to avoid signal modulations due to the inhomogeneous sensitivity of the cathode. The Continuum laser has an output energy of at least 65 mJ at 355 nm, 65 mJ at 532 nm and 100 mJ at 1064 nm. The seven-channel receiver (see Figure 2) measures the backscatter at each of the emitted wavelengths as well as the depolarization at 355 nm, the nitrogen Raman channels at 387 nm and 607 nm and the water vapor Raman channel at 407 nm. All of the channels, except the 1064 nm channel, use LICEL photomultiplier tubes coupled into a LICEL analog/photon counting transient recorder to increase the dynamic range. The 1064 nm channel is focused onto a Perkin Elmer C30956E avalanche photodiode (APD). The APD incorporates a logarithmic amplifier (25mV rms noise), made by Optech Inc., to increase dynamic range. The amplifier was calibrated prior to the experiment via a transfer function, to convert the signal to a linear scale, in addition to second-order corrections provided by Optech Inc. The signal is

directed into a 14-bit, Gage Compuscope computer card. The 1064 nm channel is generally used for qualitative information only because of issues such as APD sag and higher noise background. Both the LICEL transient recorder and Gage computer card were externally triggered by the same Stanford Research delay generator. The collected data is averaged to produce aerosol profiles from 100 m to 15 km agl every minute and water vapor profiles from 100 m to 10 km agl every 5 minutes.

3.3 Ozone DIAL design

The ozone DIAL system optical bench layout and detector design is shown in Figure 3. A dual laser design is also used for redundancy and can be engaged remotely by a user-controlled translation stage that moves the folding mirror in and out of the optical axis of the transmitter. The folding mirrors have an anti-reflection coating at 266 nm. The lasers are Continuum Inlite III Nd:YAG operating at 20 Hz with an output energy specification of 45 mJ at 266nm. The laser pumps a 1 m long CO_2-filled Raman cell (Nakazato et al., 2007) manufactured by Light Age. The two 45º mirrors together provide enough adjustment to align the laser beam to the optical axis of the Raman cell. The multi-wavelength output from the Raman cell is directed zenith by a steering mirror that is broadband coated from 266 nm to 320 nm. This 50 mm optic mounted in a Thorlabs mount with encoded Thorlab actuators has a user-controlled interface to permit remote alignment if necessary. The differential pair chosen for the DIAL is the second and third Stokes lines from the Raman conversion, namely 287 nm and 299 nm. The two wavelengths are separated out via the detector block where the signals from the LICEL photomultiplier tubes are directed into a LICEL analog/photon counting transient recorder. Again, the optical design imaged the aperture onto the photomultiplier tube for the same reason discussed in section 3.2. A slight delay is imposed on the DIAL Stanford Research delay generator to minimize cross-talk between the two LIDAR systems. The single telescope design is capable of measuring ozone as low as 400 m above ground level (agl) to altitudes reaching 15 km during the night every 5 minutes. It operates 24 hours a day, seven days a week, except during precipitation events. The system is operated remotely and the data are updated hourly to a website providing near real-time capability.

3.4 AMOLITE Ozone DIAL Algorithm and its Validation

The raw data for AMOLITE is acquired every minute with a vertical resolution of 3.75 m. The data is then averaged (10 minutes for color-coded plots and sometimes longer for individual

profiles) and processed using a boxcar filter to produce a simple smoothing of the raw data, followed by a second-order Savitzky-Golay convolution to compute the derivative with respect to altitude of the signal ratio and $\frac{\beta_{on}(z)}{\beta_{off}(z)}$. Although the Savitsky-Golay approach may cause issues at the top of the stratospheric ozone profiles (Godin et al., 1999) it does not have as much of a negative impact for tropospheric ozone due to the vertical structure of ozone typically increasing at the top of the profile. This is primarily due to the signal-to-noise ratio being large enough at most altitudes. Alternate, more sophisticated filters are being considered (Leblanc et al., 2016a) and may be implemented in future data versions, but for now all TOLNet LIDARs are using the same approach. The boxcar smoothing used on AMOLITE data is a simple first pass noise removal technique where a centered smoothing window is moved along the lidar signal profile and the average value across the window is calculated for each altitude. The averaged values then become the resulting smoothed profile. The size of the smoothing window starts at 10 bins and increases slightly with altitude (eg. window is 150 at 12 km) to compensate for the higher signal-to-noise ratio encountered at increased range. The ozone data is also dead-time corrected using a value of 4 ns. The background correction was determined by using the average background value calculated over a 10 km range starting at 35 km. For the Rayleigh extinction term we used the formulation described by Equation 2.25 from Kovalev and Eichinger, 2004. Also, the variable ozone cross sections, at the AMOLITE wavelengths, were introduced using the Brion-Daumont-Malicet (BDM) values found in Weber et al., 2016. The BDM values were interpolated onto a 0.01 nm x 0.1 K grid.

The ozone data was not corrected for SO_2 interference. There are only a few times during all the time periods presented in this paper where the ground level concentration of SO_2 was above 5 ppbv. These events generally only lasted an hour or two and were thought to be associated with the industrial plumes. Unfortunately, we did not have vertical profile information for SO_2 which can be highly variable in the lower troposphere and so these data were screened out of the ozone plots. The clouds and regions of high aerosol concentration were also screened out of the ozone plots. Discussions are underway within TOLNet to reach a consensus on how to correct the ozone DIAL profiles when aerosols are present.

When undergoing a system validation, it is important to compare the final ozone profiles between DIAL systems and determine whether the differences are instrumental and/or algorithm dependent. As a result, AMOLITE's ozone algorithm was tested against a standardized algorithm developed for the SCOOP validation campaign. The first step required

a data importer to be written that could read the simulated data into the AMOLITE algorithm. The simulated data included both the simulated LIDAR data and simulated sonde profiles. Next a boxcar smoothing that is applied to the AMOLITE data was turned off as there is no equivalent in the standardized algorithm. The algorithm testing began by turning off the dead-time correction (saturation), background correction, Savitzky-Golay smoothing, Rayleigh extinction correction and variable ozone absorption cross sections (constant values were used for both wavelengths), leaving only the bare bones ozone calculation. The concept was to use the simulated input in both the AMOLITE and standardized algorithms, comparing the results to the original simulated ozone profile with each algorithm. With all of the above terms turned off, the results matched perfectly after ensuring all unit conversions were done correctly and verified both algorithms were using the same resolution functions. The next test involved using a different simulated ozone profile with saturation turned on. Comparing this to both algorithms with dead-time correction set to 4 ns gave confidence that the algorithms were both handling the saturation effects correctly. The next test involved turning off all the terms except the Rayleigh extinction correction and testing this new simulated ozone product against both the algorithms. Once it was established that both algorithms were calculating the Rayleigh profile from the simulated sonde input, the output matched with less than a 0.05% bias, acceptable and not unexpected from math rounding errors. Proceeding to the next test, all terms were turned off except for the variable ozone absorption cross sections. Here is was important to make sure the wavelengths of the system were taken to sufficient accuracy to minimize errors in the values picked form the standardized look-up table. In our case the wavelength values were set to the AMOLITE DIAL wavelengths of 287.20 and 299.14 nm. Once again with a successful outcome the final test was to turn on random (Poisson) noise and added sky background to the simulated ozone profile. For this final test all the terms were turned off except the background correction and a second-order Savitzky-Golay convolution applied yielding a final result within 0.2%. The end result of this testing gave us confidence that the AMOLITE ozone algorithm was performing flawlessly. Details of the results and comparisons to the other TOLNet LIDAR systems will be presented in the SCOOP validation paper (manuscript in preparation).

~~3.4~~3.5 AMOLITE Instrument Validation and Calibration

The performance of the ozone LIDAR was evaluated through an inter-comparison study with four other tropospheric ozone LIDARs, all of which are part of TOLNet (Tropospheric Ozone

LIDAR Network). The campaign named SCOOP (Southern California Ozone Observation Project) took place at the JPL Table Mountain Facility in Wrightwood, California. This provided an opportunity to compare AMOLITE~~LIDAR~~ ozone profiles between other LIDAR instruments and 14 ozone sondes launched during the study. The vertical resolution of the ozone LIDAR was chosen to be range dependent to provide sufficient detail in the lower troposphere as well as providing ozone profile information to altitudes reaching the tropopause where the return signal is significantly weaker. Figure 4 shows the effective range dependent resolution obtained using the algorithm developed by Leblanc et al., 2016~~ab~~. The left y-axis shows the effective resolution during SCOOP in meters above sea level that was applied to the AMOLITE ozone data in Figure 5. Figure 5a represents a 30-minute average of the LIDAR data starting from the time of the sonde launch at 401 UTC on 10 August 2016 and Figure 5b is also a 30-minute average at 2103 UTC on 16 August 2016. These two profiles were shown to represent the typical results contrasting the range of the ozone DIAL during nighttime and daytime operation. Typically, the DIAL measurements at night~~during the nighttime~~ will reach a range of over 10 km agl ~~above ground level~~ and dip to 7 km agl ~~above ground level~~ around midday when the~~during high~~ solar background is high. The agreement between AMOLITE and the ozone sonde on both days is very good, with the LIDAR generally staying within approximately 10-2~~1~~0% of the ozone sonde values and no obvious bias throughout the profile. There are a few regions, notably around layer transitions, where the difference reaches 50%. This is often due to the difference in vertical resolution of the two instruments. Note the sonde data is plotted at the highest vertical resolution available. It is also important to note that the geophysical separation of the sonde at altitudes of 12 km above sea level is 20-30 km for these cases, which can easily account for the larger differences between the sonde and LIDAR as the altitude increases. On some days during the study the LIDAR/sonde agreement varied significantly, particularly at the higher altitudes, due to the large geophysical separation of the two measurements. This is~~can be~~ shown in Figure 6 which represents the average of all 14 LIDAR/sonde comparisons. The middle panel clearly shows that up to 8 km the lidar agrees to within 5% of the sonde, with larger differences aloft where there are fewer number of coincidences and the geophysical separation with the sonde increases.

The entire SCOOP campaign is captured in the false color ozone DIAL plot shown in Figure 7. AMOLITE was the only fully autonomous LIDAR operating during SCOOP. The advantages of a fully autonomous LIDAR system are easily recognized in its ability to capture a continuous dataset throughout the complete diurnal~~daylight~~ cycle while capturing the dynamics and mixing

of long--term events. The ozone DIAL is reaching the lower stratosphere, enabling observations of STT events. The signal-to--noise was affected 11-14 August when there was an air conditioner failure. The outside temperature was reaching over 30 C and the single remaining air conditioner was unable to keep up with the cooling demand of two LIDARs operating simultaneously. A decision was made to turn off the aerosol/water vapor LIDAR for the remainder of the study to focus on the ozone inter-comparison.

The two color-coded plots in Figure 8 show the advantage of coincident measurements of ozone and water vapor. In this case a stratospheric intrusion which starts just after 1200 UTC on 10 August, descendsmixes down to approximately 4 km above sea level and persists for over three days. The water vapor plot (see Figure 8b), even though it represents night time measurements only, clearly shows the very dry air coincident with the high ozone concentrations of the stratospheric intrusion. The water vapor measurements values below 4 km are also very interesting. Initially on 10 August show there also appears to be very dry air (and high ozone values) which may also represent a prior stratospheric intrusion, followed by a more defined boundary layer with an increase in water vapor, more typical of boundary layer air. The water vapor channel was calibrated as described by Al Basheer et al., 2015 using the SCOOP radiosonde data.

3.5 AMOLITE Algorithm Validation

When undergoing a system validation, it is important to not only compare the final ozone profiles between DIAL systems, but determine whether the differences are instrumental and/or algorithm dependent. As a result, AMOLITE's ozone algorithm was tested against a standardized algorithm developed for the SCOOP validation campaign. The first step required a data importer to be written that could read the simulated data into the AMOLITE algorithm. The simulated data included both the simulated LIDAR data and simulated sonde profiles. Next a boxcar smoothing that is applied to the AMOLITE data was turned off as there is no equivalent in the standardized algorithm. The algorithm testing began by turning off the dead-time correction (saturation), background correction, Savitzky-Golay smoothing, Rayleigh extinction correction and variable ozone absorption cross sections (constant values were used for both wavelengths), leaving only the bare bones ozone calculation. The concept was to use the simulated input in both the AMOLITE and standardized algorithms, comparing the results to

~~the original simulated ozone profile with each algorithm. With all of the above corrections turned off the results matched perfectly after ensuring all unit conversions were done correctly and verified both algorithms were using the same resolution functions. The next test involved using a different simulated ozone profile with saturation turned on. Comparing this to both algorithms with dead-time correction set to 4 ns gave confidence that the algorithms were both handling the saturation effects correctly. The next test involved turning off all the correction terms except the Rayleigh extinction correction and testing this new simulated ozone product against both the algorithms. Once it was established that both algorithms were calculating the Rayleigh profile from the simulated sonde input, the output matched with less than a 0.05% bias, acceptable and not unexpected from math rounding errors. Proceeding to the next test, all corrections turned off, but the variable ozone absorption cross sections. Here is was important to make sure the wavelengths of the system were taken to sufficient accuracy to minimize errors in the values picked form the standardized look-up table. In our case the wavelength values were set to the AMOLITE DIAL wavelengths of 287.20 nm and 299.14 nm. Once again with a successful outcome the final test was to turn on random (Poisson) noise and added sky background to the simulated ozone profile. For this final test all the corrections were turned off except the background correction and a second-order Savitzky-Golay convolution applied yielding a final result within 0.2%. The end result of this testing gave us confidence that the AMOLITE ozone algorithm was performing flawlessly. Details of the results and comparisons to the other TOLNet LIDAR systems will be presented in the SCOOP validation paper (manuscript in preparation).~~

3.6 AMOLITE Ozone Uncertainty

An uncertainty in the ozone concentration from AMOLITE can be calculated mathematically for several components. For consistency with other DIAL systems within TOLNet, the uncertainty calculation was based on the paper by Leblanc et al., 2016b~~a~~. For a detailed description of the mathematical formulations please refer to that paper. In brief, the total uncertainty determined for AMOLITE (eg. See Figures 5 and 6) was based on six different components: uncertainty due to detector noise, uncertainty due to saturation, uncertainty due to the Rayleigh cross-section, uncertainty due to the background calculation, uncertainty due to the ozone cross-section, and uncertainty due to the air number density. To calculate these uncertainties, one must also make estimates of dead time error (estimate 10%), the Rayleigh

error (estimate 1%), the sonde pressure uncertainty (estimate 20 Pa) and the temperature uncertainty (estimate 0.3K). The AMOLITE uncertainty calculations, for each individual uncertainty, successfully compared to the standardized algorithm uncertainty for a test profile. The altitude at which the AMOLITE ozone profiles get truncated is based on a total uncertainty threshold value chosen to be 15 % based on AMOLITE/sonde comparisons. There is no threshold value set for the ozone false color plots. This can sometimes provide additional context for the existence of layers, particularly at higher altitudes.

4 AMOLITE: Oski-ôtin Measurements

After the SCOOP campaign, AMOLITE was transported back to ECCC's Centre For Atmospheric Research Experiments where the air conditioning unit was repaired and routine maintenance was done on the instrument to prepare it for deployment to the oil sands region in northern Alberta. AMOLITE started collecting the full suite of data products on 3 November 2016. The instrument has run fully autonomous, collecting a year's worth of consecutive data except for a couple of weeks in July when the instrument was down for a service visit due to a laser failure, and two shorter periods of time for routine maintenance requirements. During the first year of operation, the autonomous ozone, aerosol and water vapor LIDAR measurements provided a near continuous dataset, observing the impact of many atmospheric processes and transport over a range of scales and altitudes. The following sections give examples of three selected periods throughout the year showing the impact of long-range transport events, atmospheric dynamics and local industrial sources as well as seasonal variability.

4.1 6-13 November 2016

Stratospheric intrusions were frequently observed throughout the year, with sometimes three or four occurrences per week. In recent years, there has been more understanding about the mechanism that enables these STT events (Langford et al., 2018). However, there is still very little data on the frequency and magnitude of these events and their impact on the tropospheric ozone budget. For example, Figure 9 shows three false-color plots of ozone, water vapor and aerosol backscatter ratio for the bottom 10 km of the atmospheric from 6-13 November 2016. During this week-long period two stratospheric intrusions wea~~a~~re observed (and evidence that a third ~~is~~ started~~ing~~ on the 13 November). The white areas on the ozone plot, represent cloudy regions where the DIAL system is unable to retrieve ozone values. These white areas correlate

very well with the cloud regions displayed in the aerosol backscatter ratio plot. The water vapor plot shows dry air (less than 0.2 g/kg) coincident with the higher ozone concentrations of the stratospheric air reaching down into the moist regions more typical of the lower atmosphere. During most of the stratospheric intrusions over the Oski-ôtin site, it was noted that although the free tropospheric ozone levels were increased significantly, the ozone intrusion does not always penetrate the boundary layer and increase surface values.

A series of ozone vertical profiles during the stratospheric intrusion between 9-11 November is plotted in Figure 10. This plot shows the ozone concentration before the intrusion (red line) where the typical background value of approximately 30 ppbv is present in the lowest 4 km. As time progresses, one can clearly see the high ozone concentration, reaching 120 ppbv on 10 November at 0000 UTC, from the stratospheric transport~~exchange~~ descending down to lower and lower altitudes. The impact increased the tropospheric budget by almost a factor of 2. Figure 11 shows only the lowest 4 km of the ozone plot compared to the ground level observations of ozone and NO_x. ~~Visually t~~There is reasonably good agreement between the ground level measurements and~~t~~ the DIAL measurements around 600m (the lowest few LIDAR bins can be unreliable as they are strongly dependent on the alignment and temperature fluctuations inside the trailer). It is also important to consider the height of the boundary layer (see Figure 12a) ~~and the mixing of the lowest water vapor region,~~ which during the winter time can be significantly lower. The ozone/NOx relationship in Figure 11b is not the typical diurnal relationship that can be observed, in part due to the stratospheric intrusion event, but also due to industrial plume sources impacting the site. For several hours on 7, 8 and 9 November the ozone values approach 0. There is an increase in ozone during the daytime hours (solar day is approximately 1400 to 0000 UTC during this period), but also an increase during the night time on 10, 11 and 12 November when the stratospheric intrusion occurred. Figure 12 shows the aerosol LIDAR plot for the lowest 4 km along with various chemical and particulate tracers from CAM1. The aerosol LIDAR plot gets down to approximately 100 above ground level, which during the winter months is necessary to observe the boundary layer and plume dynamics. There is a good correspondence between the increase in aerosol shown by the LIDAR and the PM2.5 trace over the entire period. The increase in particle concentration is linked to the presence of the plume impacting the site. For example, on the 7-9 November and the night of 10 November the aerosol LIDAR observations show an increase in concentration in the lowest 750 m (see Figure 12a) typically of industrial plume sources. As the plume impacts the ground directly, there is a substantial bump in the PM2.5 concentration. Figures

12c and 12d also indicate that the air is from an industrial source where the~~re is high sulphate,~~ CO_2, CO~~, and~~ CH_4 and sulfur compound concentrations are high. This is the first example where the vertical context given by the LIDAR aids in the understanding of the ground-based measurements.

4.2 29-31 August 2017

Another occurrence that can change the ozone budget is forest fires (Jaffe and Wigder, 2012). ~~Ozone production during forest fire activity is well documented and can have an impact on local air quality.~~ During the period of 29-31 August, smoke from a forest fire was advected into the region as shown in the MODIS (Moderate Resolution Imaging Spectroradiometer) true color image acquired form the Terra satellite on the 31 August 2017 (see Figure 13). The ozone plot shown in Figure 14a presents a significant amount of ozone in the free troposphere. The enhanced ozone signature on 29 August is from a stratospheric intrusion whereas the enhanced ozone on 30 and 31 August is a result of forest fire smoke. The extent of the forest fire smoke is shown ~~This can be clearly seen~~ by the large aerosol burden in Figure 14b coincident with the ozone as well as the depolarization ratio plot in Figure 14c, showing a value of about 5%, consistent with other smoke plume measurements (Aggarwal et al., 2017).~~.~~

The~~A~~ diurnal cycle of ozone over three days are~~is~~ shown in Figure 15b with increased ozone due to the smoke impacting the surface around 00 UTC 31 August, from what we hypothesize to be enhancement from the forest fire. In Figure 15a a series of ozone traces at different altitudes from the DIAL measurements are plotted against the ground ozone values. In this plot the ozone aloft tracks the ground level ozone quite well until the ozone enhanced air from the forest fire smoke begins to descend over the site. The noisy ozone values around the 1000m level are a result of an error in ozone when the aerosol concentrations were very high (see Figure 14 (a) and (b) around 1500 UTC to 1700 UTC on 31 August). There is also evidence that the smoke impacted the surface from 00 UTC – 1800 UTC on August 31st shown in Figure 15c-15e where an increase in H_2S, PM2.5 and CO also occur. ~~Figure 16 shows an overlay of the wind field from the windRASS on the LIDAR backscatter ratio plot for the bottom 1 km of the atmosphere. It shows the change in wind direction around the period where the smoke is impacting the ground site at Oski-ôtin. There is also indications that the site is being impacted by industrial sources to the south.~~

An alternative way to plot aerosol LIDAR data is to plot extinction coefficients instead of backscatter coefficients. Since we are measuring the nitrogen Raman channel during the night time, we can calculate the backscatter coefficient, extinction coefficient and extinction-~~-~~to-backscatter ratio also known as the S ratio. The S ratio is a useful quantity for determining the air ~~parcel~~ type (see Strawbridge, 2013). The three-panel plot in Figure 16~~7~~ shows the 355 nm backscatter coefficient, extinction coefficient and S ratio for 300 UTC to 1200 UTC (night time) on 31 August 2017 using 10-minute average data. The near field overlap is corrected and the data are plotted in kilometers above mean sea level (msl), primarily because the atmospheric density obtained from sonde data is also relative to msl. The white noisy regions aloft on the extreme left and right are artifacts due to the increase in sky background. The backscatter coefficient plot reveals the dynamic nature of the smoke plume between 1 to 5 km and a cirrus cloud layer between 8.5 to 11 km. The extinction coefficient plot is useful because one can directly relate it to aerosol optical depth by integrating along the altitude range. The S ratio plotted as a 10-minute average shows extraordinary detail within the smoke plume with values ranging approximately from 40 to 65 sr. These values are consistent with the value of 45 to 65 sr reported by Barbosa et al. (2014) and are consistent with several other observations provided in Table 3 of Ortiz-Amezcua et al. (2017). Figure 16~~7~~ also shows the boundary layer aerosols with an S ratio of 20 to 35 sr, indicative of larger particles in the moist boundary layer air (see water vapor plot in Figure 14d) and 10 to 15 sr in the cirrus cloud. ~~A more typical plot in the literature is to show a one-hour average S ratio.~~ Figure 17~~8~~ shows a one-hour average taken between 800 UTC and 900 UTC. For highly variable conditions such as a forest fire plume, the one-hour average may result in underestimating the maximum S value. It is also very difficult to measure the S value in the free troposphere when there is very little aerosol present, such as in this case. Those values will be very noisy and have been discriminated out of the dataset shown here.~~ Applying a night time S ratio profile, particularly on features like forest fire plumes and cirrus clouds, can greatly improve the daytime product over using standard look-up table S values for different air types.~~

4.3 4-9 September 2017

The ozone plot for 4-9 September 2017 (see Figure 18~~9~~a) shows~~has~~ several processes occurring throughout the entire altitude range. There is a stratospheric intrusion on 4 September that extends into 5 September (see dry air in Figure 18~~9~~d). The increased ozone in the free

troposphere from 6-9 September is due to the forest fire activity being advected back into the region. The forest fire smoke is clearly visible in the aerosol backscatter plot (see Figure 189b) and the depolarization ratio plot (see Figure 189c). There is also a fairly dominant feature between 800 m – 2200 m where the ozone values reach very close to 0. There are also time periods where these near 0 ozone features appear to reach closer to ground level (. For example, around 1200 UTC on each day during the 4-78 September period)., the DIAL ozone approaches 0 ppbv. However, on 4 and 5 September, the very low ozone levels remain close to the ground, unlike 6-8 September, where the low ozone levels extend from 400m to 2000m. This is also shown in Figure 1920a where the ozone values from the DIAL at 500 m, 700 m and 900 m are plotted against the ground level ozone. The very low surface ozone around 1200 UTC on 7 September remains low well up into the lower troposphere. The low ozone datalevels around 1200 UTC on 8 September areis an artifact due to the very high aerosol loading and have been removed. The surface ozone levels (see Figure 1920b) on 4 September 4 ranged from a low of 10 ppbv around 1200 UTC to 20 ppbv. Figure 201 shows the winds were primarily coming from the north, where there are fewer industrial sources to impact the ground site. However, on 5 September the winds are coming from the south where the industrial sources are impacting the site as shown by the increase in NO_x (see Figure 1920b), sulphates (see Figure 1920c), PM2.5 (see Figure 1920d) and CO_2 (see Figure 1920e).

The ground level ozone increaseding to 7050 ppbv around 1800 UTC on 7 September, and droppeding to 5035 ppbv around 300 UTC on 8 September which was is mostly due to the southerly wind (see Figure 201) bringing the industrial plumes to the ground site. The DIAL ozone shows ozone levels reaching 80 ppbv within 500 m of the surface. There is also an increase in SO_4 and CH_4 during this time period. The diurnal ozone cycle is very well established throughout this entire study period, except when the elevated ozone from the forest fire smoke is mixed down to the surface starting around 600 UTC on 8 September (note the increase in NO_2 ,but no NO). The increase in ground level ozone throughout the night time reaches values of up to 3525 ppbv. There is also a steep increase in PM2.5 levels (from 25 to 50 μgm^{-3}) and CO around 1500 UTC on 8 September coincident with the LIDAR backscatter ratio plot shown in Figure 189b indicative of an increased concentration of the biomass burning plume impacting the ground site. The wind has also shifted from a southerly flow to eventually a northerly flow. The resultant ozone at the ground is a mixture of local chemistry and ozone rich air transported into the region.

A plot of the backscatter coefficient, extinction coefficient and S ratio from 7-9 September (see Figure 212) shows the contrast between the smoke plume on 8 September and the boundary layer aerosols and industrial plume (around 2 km on 7 September). The smoke plume S ratios are slightly smaller (35 to 55 sr) compared to 31 August, likely indicative of more aged smoke, (see the one-hour average plot between 1000 UTC and 1100 UTC shown in Figure 2223c). The LIDAR ratio, S, can also be calculated for 532 nm. However, there is significantly less signal-to-noise so the 10-minute average false color plots were not produced. A comparison was made for a one-hour average whenduring the smoke plumes that were present on 31 August and 8 September (see Figure 2334a and 2334b). The S ratio for 532 nm on 31 August ranges between 40 to >100 sr while on 8 September ranges between 40 to 70 sr. These values are consistent with the higher 532 nm S ratio values reported in Table 3 of Ortiz-Amezcu et al. (2017). The advantage of having an S ratio at two wavelengths, is that one can now calculate the Angstrom exponent (see Figure 24c and 24d). The Angstrom exponent (see Figure 23c and 23d) is inversely related to the average size of the particles. On 31 August the Angstrom exponent was 1.56 +- 0.2 between 2 to 4.2 km in contrast to 1.35 +- 0.2 between the 2 to 4 km 8 September. These values are consistent with what others have reported for biomass burning (see Table 3 by Ortiz-Amezcu et al. (2017)). During this six-day period it would be very difficult to understand the ground measurements without the vertical context of the LIDARs.

5 Conclusions and future work

Environment Canada has successfully designed, built and deployed a fully autonomous ozone, aerosol and water vapor LIDAR system called AMOLTE. The instrument participated in a validation campaign with other tropospheric ozone LIDARs where the continuous operation of AMOLITE provided a unique dataset showing the complete evolution of atmospheric events. The instrument underwent an extensive validation in both the hardware and software algorithm processing to provide confidence in the AMOLITE ozone profiles generated. A comparison with ozone sondes revealed no bias in the AMOLITE ozone profile and typical difference of less than 10 % throughout the altitude range. It was also shown that stratospheric intrusions can have frequent and significant impact on free tropospheric and sometimes even surface measurements. In some cases the ozone concentration at the surface can be increased by a

factor of 2. It was also shown that higher ozone levels in forest fire plumes can also impact local air quality. The lidar ratio was also calculated for the forest fire plume and found to range between 35 to 65 sr at 355 nm and 40 to 100 sr at 532 nm. It was also noted that over an eight-day period the S ratio decreased. The average Angstrom exponent went from 1.56 on 31 August to 1.35 on 8 September. The three-LIDAR system provides critical information and vertical context to help interpret ground-based surface measurements. The primary motivation in building AMOLITE, was to collect continuous LIDAR profiles, except during precipitation, to improve our understanding of the impact and extent of long-range transport and other pollution events on air quality at local, regional and national scales. Developing an autonomous LIDAR facility significantly reduces the operational field costs of maintaining on site personnel. The development of the instrument was possible due to recent technological advancements in laser technology and internet-controlled electronics. A sophisticated control program was developed to provide safe operations, extensive system controls and the storage, transmission and display of the data in near real-time. One of the challenges with an autonomous multi-LIDAR system is the large volume of data produced. While the quick look products that are currently produced are very useful to survey data quality and periods of interest in will be necessary to develop algorithms to meet the data archival needs and produce various product data levels. Some of these will include automated cloud screening, aerosol corrections and possibly other derived products such as boundary layer height. The implementation of these algorithms in the future will provide further value~~a valuable dataset~~ for the current location as well as future observation sites.

Current plans are underway to add a second telescope to the ozone DIAL to allow measurements closer to the surface. A couple of different designs are being investigated that will fill in the gap between 100 m to 500 m. This is quite important, particularly during the winter months and night time operation, when the boundary layer can often be less than 500 m in height.

Acknowledgements

The project was supported by the Environment and Climate Change Canada's Climate Change and Air Quality Program (CCAP) and the Joint Oil Sands Monitoring program (JOSM).

References

Aggarwal, M., Whiteway, J., Seabrook, J., Gray, L., Strawbridge, K., Liu, P., O'Brien, J., Li, S.-M., and McLaren, R.: Airborne Lidar Measurements of Aerosol and Ozone Above the Canadian Oil Sands Region, Atmos. Meas. Tech. Discuss., https://doi.org/10.5194/amt-2017-391, in review, 2017.

Al-Basheer, W. and Strawbridge, K.B., Lidar vertical profiling of water vapor and aerosols in the Great Lakes Region: A tool for understanding lower atmospheric dynamics, J. Atmospheric Sol.-Terr. Phys., 123, 144-152, 2015. doi: 10.1016/j.jastp.2015.01.005

Ancellet, G., Pelon, J., Beekmann, M., Papayannis, A., and Megie, G.: Ground-based lidar studies of ozone exchanges between the stratosphere and troposphere, J. Geophys. Res., 99, D12, 22401-22421, 1991.

~~Ansmann, A., Riebesell, M. and Weitkamp, C.: Measurements of atmospheric aerosol extinction profiles with a Raman lidar, Opt. Lett. 15, 746-748, 1990.~~

Ashmore, M. R., Assessing the future global impacts of ozone on vegetation. Plant, Cell & Environment, 28: 949–964, 2005. doi:10.1111/j.1365-3040.2005.01341.x

~~Aspey, R. A., McDermid, I. S., Leblanc, T., Walsh, D. and Howe, J.: New Raman water vapor and temperature lidar at JPL table mountain facility: optimization, validations and sonde intercomparison, Proc. SPIE Lidar Remote Sensing Conference, Stockholm, Sweden, 11-14 September 2006, 63670A, 2006.~~

Baray, J.-L., Courcoux, Y., Keckhut, P., Portafaix, T., Tulet, P., Cammas, J.-P., Hauchecorne, A., Godin Beekmann, S., De Mazière, M., Hermans, C., Desmet, F., Sellegri, K., Colomb, A., Ramonet, M., Sciare, J., Vuillemin, C., Hoareau, C., Dionisi, D., Duflot, V., Vérèmes, H., Porteneuve, J., Gabarrot, F., Gaudo, T., Metzger, J.-M., Payen, G., Leclair de Bellevue, J., Barthe, C., Posny, F., Ricaud, P., Abchiche, A., and Delmas, R.: Maïdo observatory: a new high-altitude station facility at Reunion Island (21° S, 55° E) for long-term atmospheric remote sensing and in situ measurements, Atmos. Meas. Tech., 6, 2865-2877, https://doi.org/10.5194/amt-6-2865-2013, 2013.

Barbosa, H. M. J., Barja, B., Pauliquevis, T., Gouveia, D. A., Artaxo, P., Cirino, G. G., Santos, R. M. N., and Oliveira, A. B.: A permanent Raman lidar station in the Amazon: description,

characterization, and first results, Atmos. Meas. Tech., 7, 1745-1762, https://doi.org/10.5194/amt-7-1745-2014, 2014.

Bock, O., Bosser, P., Bourcy, T., David, L., Goutail, F., Hoareau, C., Keckhut, P., Legain, D., Pazmino, A., Pelon, J., Pipis, K., Poujol, G., Sarkissian, A., Thom, C., Tournois, G., and Tzanos, D.: Accuracy assessment of water vapour measurements from in situ and remote sensing techniques during the DEMEVAP 2011 campaign at OHP, Atmos. Meas. Tech., 6, 2777-2802, https://doi.org/10.5194/amt-6-2777-2013, 2013.

Clough, S. A., Iacono, M. J. and Moncet, J. L.: Line-by-line calculation of atmospheric fluxes and cooling rates: application of water vapor, J. Geophys. Res. 97, 761-785, 1992.

~~Ortiz-Amezcua, P., Guerrero-Rascado, J. L., Granados-Muñoz, M. J., Benavent-Oltra, J. A., Böckmann, C., Samaras, S., Stachlewska, I. S., Janicka, Ł., Baars, H., Bohlmann, S., and Alados-Arboledas, L.: Microphysical characterization of long-range transported biomass burning particles from North America at three EARLINET stations, Atmos. Chem. Phys., 17, 5931-5946, https://doi.org/10.5194/acp-17-5931-2017, 2017.~~

Dionisi, D., Congeduti, F., Liberti, G. L. and Cardillo, F.: Calibration of a multichannel water vapor Raman lidar through noncollocated operational soundings: optimization and characterization of accuracy and variability, J. Atmos. Ocean. Tech. 27, 108-121, 2009.

Feingold, G., Eberhard, W. L., Veron, D. E., and Previdim M.: First measurements of the Twomey indirect effect using ground-based remote sensors, Geophy. Res. Lett., 30, 1287, 2003.

Gaudel, A., Ancellet, G., Godin-Beekmann, S.: Analysis of 20 years of tropospheric ozone vertical profiles by lidar and ECC at Observatoire de Haute Provence (OHP) at 44°N, 6.7°E, Atmos. Environ., 113, 78-89, 2015. https://doi.org/10.1016/j.atmosenv.2015.04.028

Gaudel A, Cooper OR, Ancellet G, Barret B, Boynard A, Burrows JP, et al. . Tropospheric Ozone Assessment Report: Present-day distribution and trends of tropospheric ozone relevant to climate and global atmospheric chemistry model evaluation . Elem Sci Anth . 6 (1), 39, 2018. DOI: http://doi.org/10.1525/elementa.291

Godin, S., Carswell, A.I., Donovan, D.P., Claude, H., Steinbrecht, W.,McDermid, I.S., McGee, T.,Gross, M.R., Nakane, H., Swart, D.P.J, Bergwerff, H.B., Uchino, O., von der Gathen, P. and Neuber, R.: Ozone differential absorption lidar algorithm intercomparison, Appl. Opt. **38**, 6225-6236, 1999.

Goldsmith, J. E. M., Blair, F. H., Bisson, S. E. and Turner, D. D.: Turn-key Raman lidar for profiling atmospheric water vapor, clouds, and aerosols, Appl. Optics, 37, 4979-4990, 1998.

Granados-Muñoz, M. J. and Leblanc, T.: Tropospheric ozone seasonal and long-term variability as seen by lidar and surface measurements at the JPL-Table Mountain Facility, California, Atmos. Chem. Phys., 16, 9299-9319, https://doi.org/10.5194/acp-16-9299-2016, 2016.

Grant, W. B.: Differential absorption and Raman lidar for water vapor profile measurements: a review, Opt. Eng., 31, 40-48,1991.

Jaffe, D.A and Wigder, N.L.: Ozone production from wildfires: A critical review, Atmos. Environ., 51, 1-10, 2012. https://doi.org/10.1016/j.atmosenv.2011.11.063.

Khaykin, S. M., Godin-Beekmann, S., Keckhut, P., Hauchecorne, A., Jumelet, J., Vernier, J.-P., Bourassa, A., Degenstein, D. A., Rieger, L. A., Bingen, C., Vanhellemont, F., Robert, C., DeLand, M., and Bhartia, P. K.: Variability and evolution of the midlatitude stratospheric aerosol budget from 22 years of ground-based lidar and satellite observations, Atmos. Chem. Phys., 17, 1829-1845, https://doi.org/10.5194/acp-17-1829-2017, 2017.

Kousha, T. and Valacchi, G.: The air quality health index and emergency department visits for urticaria in Windsor, Canada, J. Toxicol. Envron. Heatlh, 78 (8), 524-533, 2015. https://doi.org/10.1080/15287394.2014.991053.

Kovalev, V. and McElroy, J.: Differential absorption lidar measurement of vertical ozone profiles in the troposphere that contains aerosol layers with strong backscattering gradients: a simplified version, Appl. Opt., 33(36), 8393-8401, 1994.

Kovalev, V.A and Eichinger, W.E.: Elastic Lidar Theory, Practice, and Analysis Methods. John Wiley & Sons, Inc., New Jersey, 2004.

Langford, A.O., Masters, C.D., Proffittm M.H., Hsie, E.-Y. and Tuck, A.F.: Ozone measurements in a tropopause fold associated with a cut-off low system, Geophys. Res. Lett., 23 (18), 2501-2504, 1996.

Langford, A.O., Alvarez, R.J., Brioude, J., Evan, S., Iraci, L.T., Kirgis, G., Kuang, S., Leblanc, T., Newchurch, M.J., Pierce, R.B., Senff, C.J. and Yates, E.L.: Coordinated profiling of stratospheric intrusions and transported pollution by the Tropospheric Ozone Lidar Network (TOLNet) and NASA Alpha Jet experiment (AJAX): Observations and comparison to

HYSPLIT, RAQMS, and FLEXPART, Atmos. Environ., 174. 1-14. 2018. https://doi.org/10.1016/j.atmosenv.2017.11.031

Leblanc, T., Walsh, T. D., McDermid, I. S., Toon, G. C., Blavier, J.-F., Haines, B., Read, W. G., Herman, B., Fetzer, E., Sander, S., Pongetti, T., Whiteman, D. N., McGee, T. G., Twigg, L., Sumnicht, G., Venable, D., Calhoun, M., Dirisu, A., Hurst, D., Jordan, A., Hall, E., Miloshevich, L., Vömel, H., Straub, C., Kampfer, N., Nedoluha, G. E., Gomez, R. M., Holub, K., Gutman, S., Braun, J., Vanhove, T., Stiller, G., and Hauchecorne, A.: Measurements of Humidity in the Atmosphere and Validation Experiments (MOHAVE)-2009: overview of campaign operations and results, Atmos. Meas. Tech., 4, 2579-2605, https://doi.org/10.5194/amt-4-2579-2011, 2011.

Leblanc, T., Sica, R. J., van Gijsel, J. A. E., Godin-Beekmann, S., Haefele, A., Trickl, T., Payen, G., and Gabarrot, F.: Proposed standardized definitions for vertical resolution and uncertainty in the NDACC lidar ozone and temperature algorithms – Part 1: Vertical resolution, Atmos. Meas. Tech., 9, 4029-4049, https://doi.org/10.5194/amt-9-4029-2016, 2016a.

Leblanc, T., Sica, R. J., van Gijsel, J. A. E., Godin-Beekmann, S., Haefele, A., Trickl, T., Payen, G., and Liberti, G.: Proposed standardized definitions for vertical resolution and uncertainty in the NDACC lidar ozone and temperature algorithms – Part 2: Ozone DIAL uncertainty budget, Atmos. Meas. Tech., 9, 4051-4078, https://doi.org/10.5194/amt-9-4051-2016, 2016b.

Li, C., Martin, R. V., Boys, B. L., van Donkelaar, A., and Ruzzante, S.: Evaluation and application of multi-decadal visibility data for trend analysis of atmospheric haze, Atmos. Chem. Phys., 16, 2435-2457, https://doi.org/10.5194/acp-16-2435-2016, 2016.

Lippmann, Morton: Health effects of tropospheric ozone, Environ. Sci. Technol., 25 (12), 1954-1962, 1991. DOI: 10.1021/es00024a001

Malley, C. S., Heal, M. R., Mills, G., and Braban, C. F.: Trends and drivers of ozone human health and vegetation impact metrics from UK EMEP supersite measurements (1990–2013), Atmos. Chem. Phys., 15, 4025-4042, https://doi.org/10.5194/acp-15-4025-2015, 2015.

McKee, David J., Tropospheric ozone human health and agricultural impacts: Lewis Publishers, Boca Raton, FL, 1994.

Nakazato, M., Nagai, T., Sakai, T., and Hirose, Y.: Tropospheric ozone differential-absorption lidar using stimulated Raman scattering in carbon dioxide, Appl. Opt., 46(12), 2269-2279, 2007.

Ortiz-Amezcua, P., Guerrero-Rascado, J. L., Granados-Muñoz, M. J., Benavent-Oltra, J. A., Böckmann, C., Samaras, S., Stachlewska, I. S., Janicka, Ł., Baars, H., Bohlmann, S., and Alados-Arboledas, L.: Microphysical characterization of long-range transported biomass burning particles from North America at three EARLINET stations, Atmos. Chem. Phys., 17, 5931-5946, https://doi.org/10.5194/acp-17-5931-2017, 2017.

Papayannis, A., Amiridis, V., Mona, L., Tsaknakis, G., Balis, D., Bösenberg, J., Chaikovski, A., De Tomasi, F., Grigorov, I., Mattis, I., Mitev, V., Müller, D., Nickovic, S., Pérez, C., Pietruczuk, A., Pisani, G., Ravetta, F., Rizi, V., Sicard, M., Trickl, T., Wiegner, M., Gerding, M., Mamouri, R. E., D'Amico, G. and Pappalardo, G.: Systematic lidar observations of Saharan dust over Europe in the frame of EARLINET (2000–2002), J. Geophys. Res., 113(D120), 148-227, 2008, doi: 10.1029/2007JD009028.

Pruppacher, H. R. and Klett, J. D.: Microphysics of Clouds and Precipitation, Kluver Academic Publishers, Dordrecht, Netherlands, 1997.

Ramanathan, V., Crutzen, P.J., Kiehl, J.T., and Rosenfeld, D.: Aerosols, climate, and the hydrological cycle, Science, 294, 2119-2124, 2001.

Singh, A., Bloss, W. J., and Pope, F. D.: 60 years of UK visibility measurements: impact of meteorology and atmospheric pollutants on visibility, Atmos. Chem. Phys., 17, 2085-2101, https://doi.org/10.5194/acp-17-2085-2017, 2017.

Sinha, A. and Harries, J. E.: Water vapor and greenhouse trapping: the role of far infrared absorption, Geophys. Res. Lett., 22, 2147-2150, 1995.

Stohl, A., and Trickl, T, A textbook example of long-range transport: Simultaneous observation of ozone maxima of stratospheric and North American origin in the free troposphere over Europe, J. Geophys. Res., 104(D23), 30445–30462, 1999, doi: 10.1029/1999JD900803.
Sugimoto, N. and Uno, I.: Observation of Asian dust and air-pollution aerosols using a network of ground-based lidars (ADNet): Realtime data processing for validation/assimilation of chemical transport models, IOP Conf. Ser.: Earth and Environ. Sci., 7, 012003, 2009, doi:10.1088/1755-1307/7/1/012003.

Strawbridge, K. B.: Developing a portable, autonomous aerosol backscatter lidar for network or remote operations, Atmos. Meas. Tech., 6, 801-816, https://doi.org/10.5194/amt-6-801-2013, 2013.

~~Trickl, T., Vogelmann, H., Giehl, H., Scheel, H.-E., Sprenger, M., and Stohl, A.: How stratospheric are deep stratospheric intrusions?, Atmos. Chem. Phys., 14, 9941-9961, https://doi.org/10.5194/acp-14-9941-2014, 2014.~~

Trickl, T., Vogelmann, H., Flentje, H., and Ries, L.: Stratospheric ozone in boreal fire plumes – the 2013 smoke season over central Europe, Atmos. Chem. Phys., 15, 9631-9649, https://doi.org/10.5194/acp-15-9631-2015, 2015.

Trickl, T., Vogelmann, H., Fix, A., Schäfler, A., Wirth, M., Calpini, B., Levrat, G., Romanens, G., Apituley, A., Wilson, K. M., Begbie, R., Reichardt, J., Vömel, H., and Sprenger, M.: How stratospheric are deep stratospheric intrusions? LUAMI 2008, Atmos. Chem. Phys., 16, 8791-8815, https://doi.org/10.5194/acp-16-8791-2016, 2016.

Twomey, S., The influence of pollution on the short wave albedo of clouds, J. Atmos. Sci., 34, 1149–1152, 1977.

Twomey, S.: Aerosols, clouds and radiation, Atmos. Environ. 25A, 2435-2442, 1991.

Uno, I., Eguchi, K., Yumimoto, K., Takemura, T., Shimizu, A., Uematsu, M., Liu, Z., Wang, Z., Hara, Y., and Sugimoto, N.: Asian dust transported one full circuit around the globe, Nat. Geosci., 2, 557-560, 2009.

Vogelmann, H., Sussmann, R., Trickl, T., and Reichert, A.: Spatiotemporal variability of water vapor investigated using lidar and FTIR vertical soundings above the Zugspitze, Atmos. Chem. Phys., 15, 3135-3148, https://doi.org/10.5194/acp-15-3135-2015, 2015.

~~Wandinger, U.: Introduction to lidar, in Lidar -Range-resolved optical remote sensing of the atmosphere, C. Weitkamp (Ed.), Springer, New York, 2005.~~

Weber, M., Gorshelev, V., and Serdyuchenko, A.: Uncertainty budgets of major ozone absorption cross sections used in UV remote sensing applications, Atmos. Meas. Tech., 9, 4459-4470, https://doi.org/10.5194/amt-9-4459-2016, 2016.

Whiteman, D.N., Melfi, S.H. and Ferrare, R.A.: Raman lidar system for the measurement of water vapor and aerosols in the Earth's atmosphere, Appl. Opt. 31, 3068-3082, 1992.

Whiteman, D. N.: Examination of the traditional Raman lidar technique II. Evaluating the ratios for water vapor and aerosols, Appl. Opt., 42, 2593-2608, 2003.

Yamamoto, G., Tanaka, M. and Kamitani, K.: Radiative transfer in water clouds in the 10-micron window region, J. Atmos. Sci. 23, 305-313, 1966.

List of Figures:

Figure 11. (a) False color plot showing of DIAL ozone from AMOLITE between 6-13 November and (b) surface measurements of ozone and NOx during the same time period.

Figure 12. (a) False color plot of aerosol backscatter ratio for the same altitude and time period as Figure 11a. CAM1 surface measurements during the same time period for (b) PM2.5 (c) sulphates and (d) CH_4, CO, CO_2 and NO.

Figure 13. Terra MODIS true color composite image on 31 August 2017. Note the location of the ground site.

Figure 14. False color LIDAR plots for 29-31 August for (a) ozone (b) backscatter ratio, (c) depolarization ratio and (d) water vapor (night time only).

Figure 15. (a) DIAL ozone traces at different altitudes compared to surface ozone for the same period as Figure 14. CAM1 surface measurements for same time period of (b) ozone and NOx (c) sulfur compounds~~PM2.5~~ (d) PM2.5~~sulphates~~ and (e) CH_4, CO, CO_2 and NO.

~~Figure 16. WindRASS data overlaid on 29-31 August AMOLITE aerosol backscatter ratio plot.~~

Figure 16~~7~~. Three-panel plot showing the backscatter coefficient ~~(scale = 0 to 20)~~, extinction coefficient ~~(scale = 0 to 1)~~ and S ratio ~~(scale = 1 to 100)~~ for 31 August. ~~Only one color bar scale was shown for simplicity.~~

Figure 17~~8~~. One-hour average between 800 UTC and 900 UTC on 31 August for (a) backscatter coefficient (b) extinction coefficient (c) S ratio (d) effective resolution.

Figure 18~~9~~. False color LIDAR plots for 4 – 9 September for (a) ozone (b) backscatter ratio, (c) depolarization ratio and (d) water vapor (night time only).

Figure ~~20~~19. (a) DIAL ozone traces at different altitudes compared to surface ozone for the same period as Figure 18~~9~~. CAM1 surface measurements for same time period of (b) ozone and NOx (c) sulfur compounds~~PM2.5~~ (d) PM2.5~~sulphates~~ and (e) CH_4, CO, CO_2 and NO.

Figure 20~~1~~. WindRASS data overlaid on 4-9 September AMOLITE aerosol backscatter ratio plot.

Figure 21~~2~~. False color plots of 4-9 September for (a) backscatter coefficient ~~(scale = 0 to 40)~~, (b) extinction coefficient ~~(scale = 0 to 2)~~ and (c) S ratio ~~(scale = 1 to 100)~~.

Figure 2~~3~~. One-hour average between 1000 UTC and 1100 UTC on 8 September for (a) backscatter coefficient (b) extinction coefficient and (c) S ratio. The effective resolution is the same as Figure 1~~8~~.

Figure 2~~4~~. (a) S ratio plot of 355 nm and 532 nm for 31 August (b) S ratio plot of 355 nm and 532 nm for 8 September (c) Angstrom exponent for 31 August and (d) Angstrom exponent for 8 September. Same one-hour averages as Figures 1~~8~~ and 2~~3~~.

1 Fig. 1 (a)

2

3 (b)

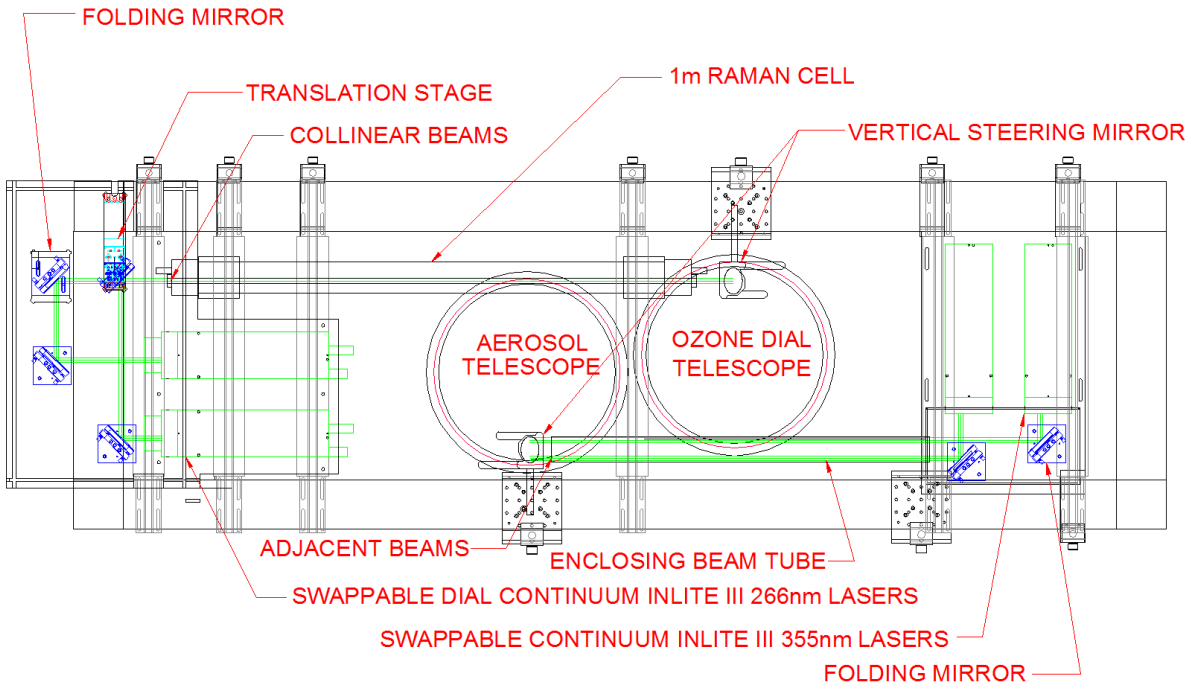

4

5

1 Fig. 2

2

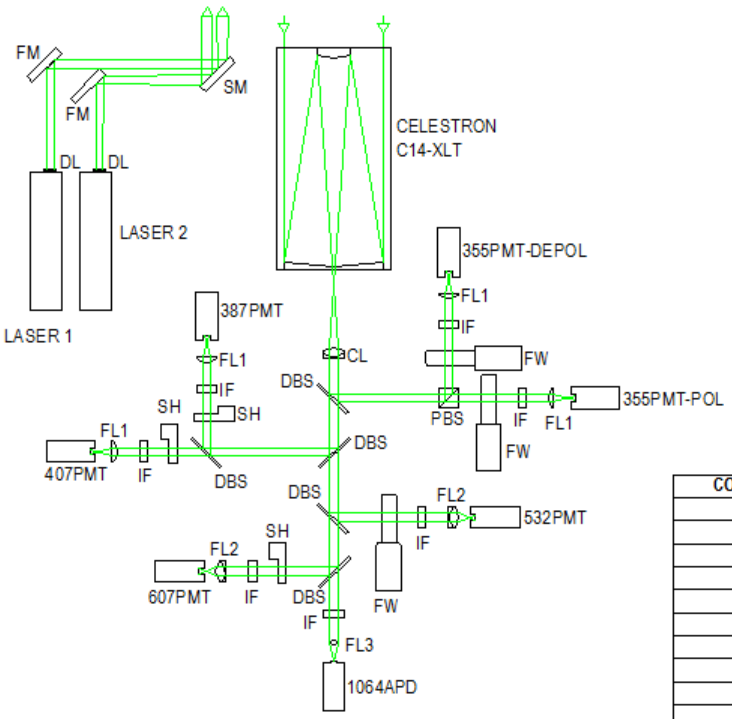

COMPONENT	DESCRIPTION
DL	DIVERGING LENS
FM	FOLDING MIRROR
SM	STEERING MIRROR
CL	ACHROMAT COLLIMATING LENS
DBS	DICHROIC BEAM-SPLITTER
PBS	POLARIZING BEAM-SPLITTER
FW	FILTER WHEEL
IF	INTERFERENCE FILTER
FL1	PLANO-CONVEX FOCUS LENS
PMT	PHOTOMULTIPLIER TUBE
FL2	ACHROMAT FOCUS LENS
SH	SHUTTER
FL3	BI-CONVEX FOCUS LENS
APD	AVALANCHE PHOTO-DIODE

3

Fig. 3

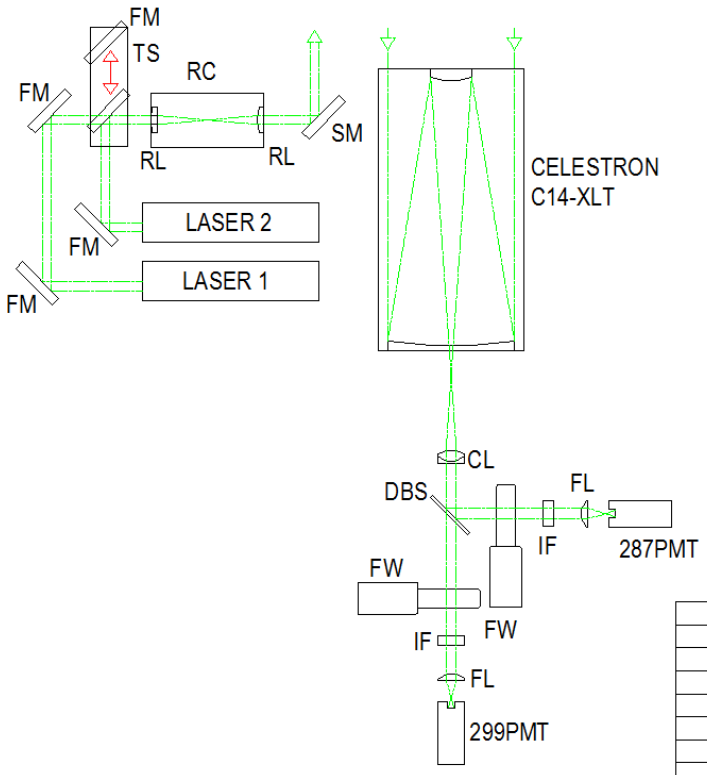

COMPONENT	DESCRIPTION
FM	FOLDING MIRROR
TS	TRANSLATION STAGE
RC	RAMAN CELL
RL	PLANO-CONVEX RAMAN LENS
SM	STEERING MIRROR
CL	ACHROMAT COLLIMATING LENS
DBS	DICHROIC BEAM-SPLITTER
FW	FILTER WHEEL
IF	INTERFERENCE FILTER
FL	PLANO-CONVEX FOCUS LENS
PMT	PHOTOMULTIPLIER TUBE

1 Fig. 4

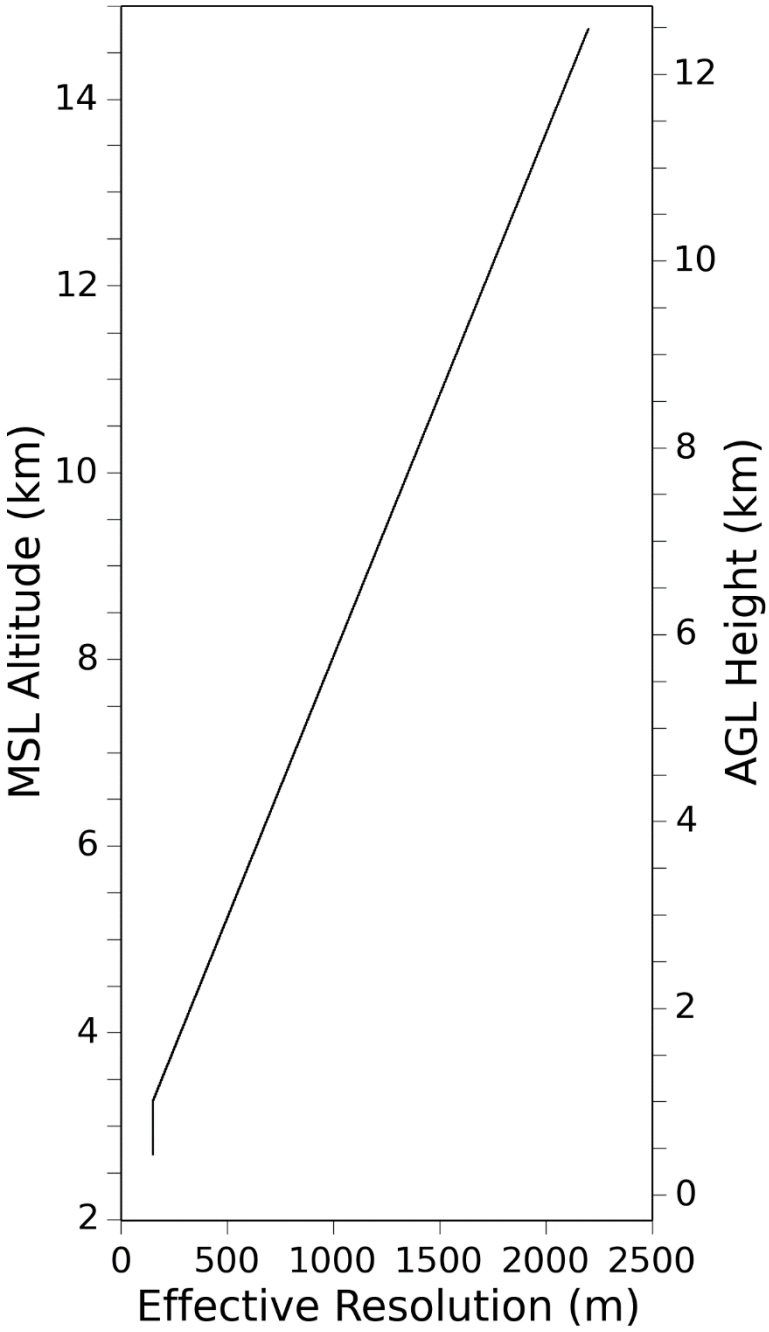
MSL Altitude (km)
AGL Height (km)
Effective Resolution (m)
2
4
6
8
10
12
14
0
2
4
6
8
10
12
0
500
1000
1500
2000
2500

2

Fig. 5 (a)

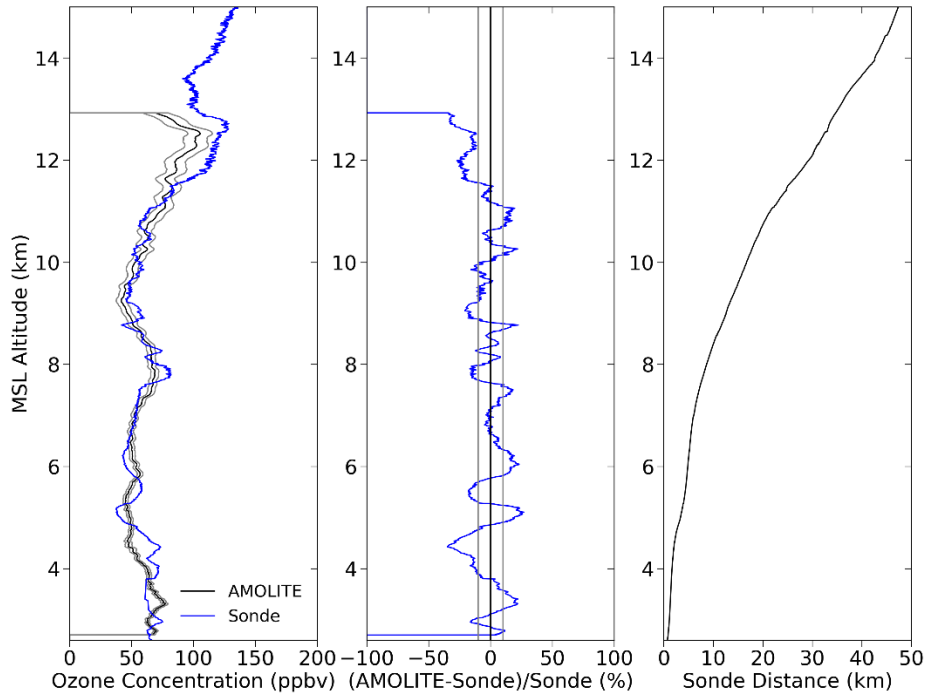
MSL Altitude (km)
AMOLITE
Sonde
Ozone Concentration (ppbv)
(AMOLITE-Sonde)/Sonde (%)
Sonde Distance (km)

(b)

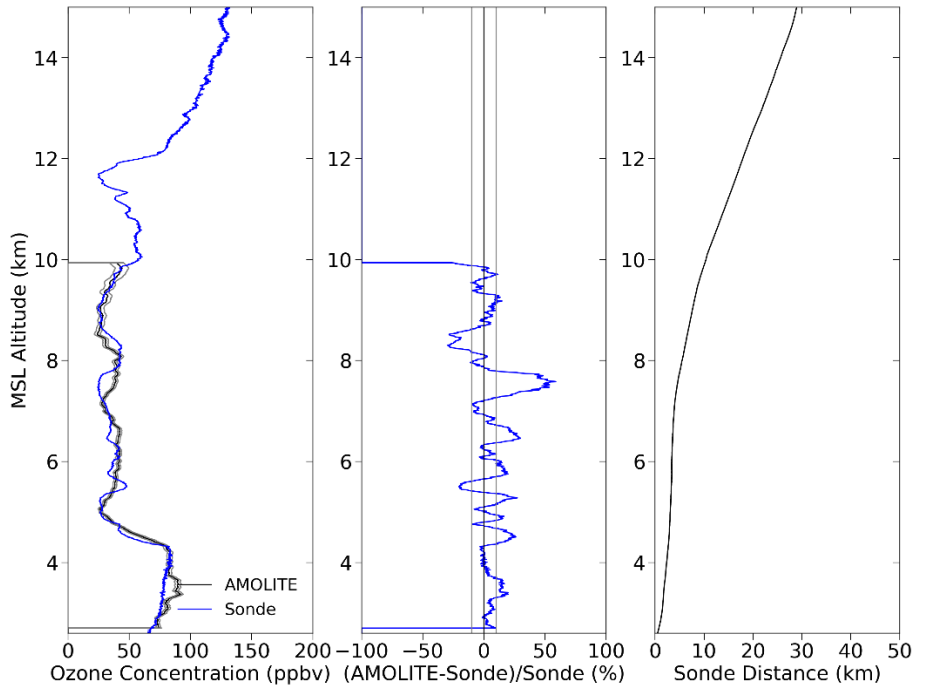
MSL Altitude (km)
AMOLITE
Sonde
Ozone Concentration (ppbv)
(AMOLITE-Sonde)/Sonde (%)
Sonde Distance (km)

Fig. 6

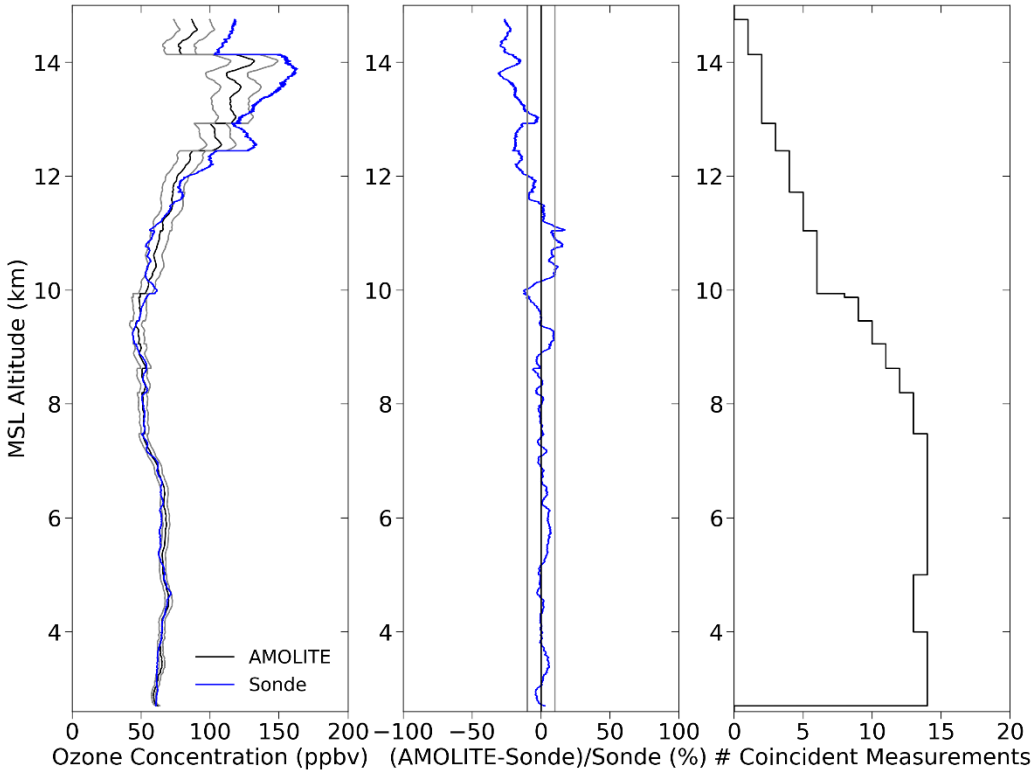
MSL Altitude (km)
14
12
10
8
6
4
AMOLITE
Sonde
0
50
100
150
200
Ozone Concentration (ppbv)
−100
−50
0
50
100
(AMOLITE-Sonde)/Sonde (%)
0
5
10
15
20
Coincident Measurements

Fig. 7

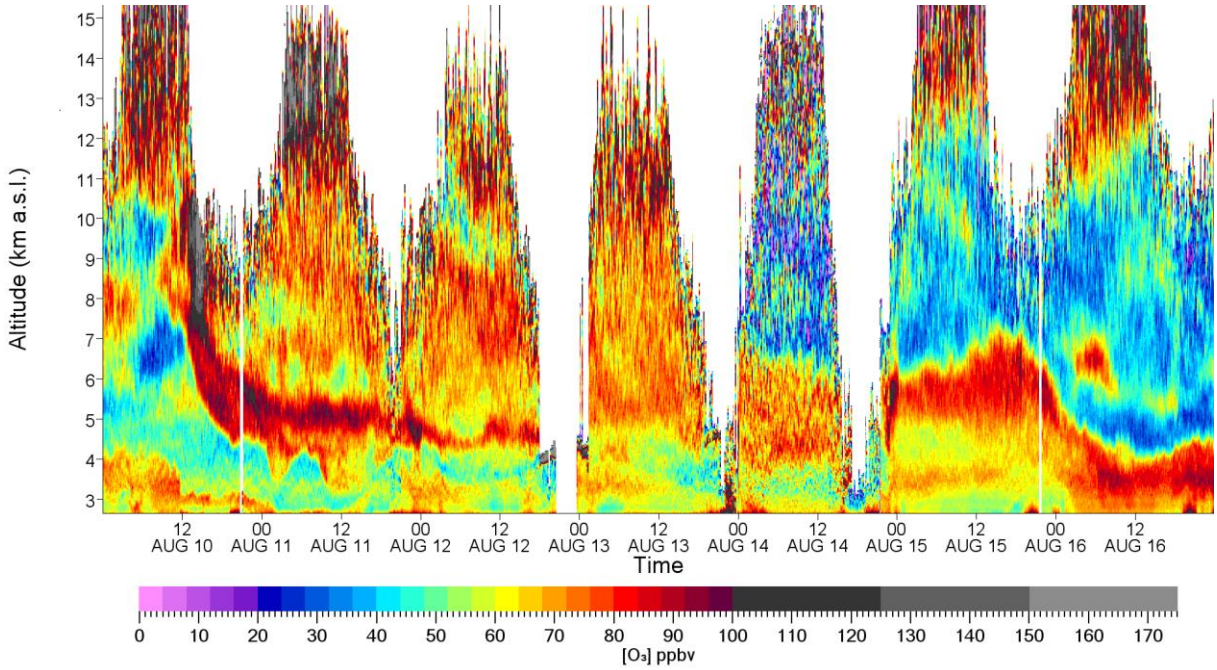
Altitude (km a.s.l.)
15
14
13
12
11
10
9
8
7
6
5
4
3
12 AUG 10
00 AUG 11
12 AUG 11
00 AUG 12
12 AUG 12
00 AUG 13
12 AUG 13
00 AUG 14
12 AUG 14
00 AUG 15
12 AUG 15
00 AUG 16
12 AUG 16
Time
0 10 20 30 40 50 60 70 80 90 100 110 120 130 140 150 160 170
[O3] ppbv

Fig. 8

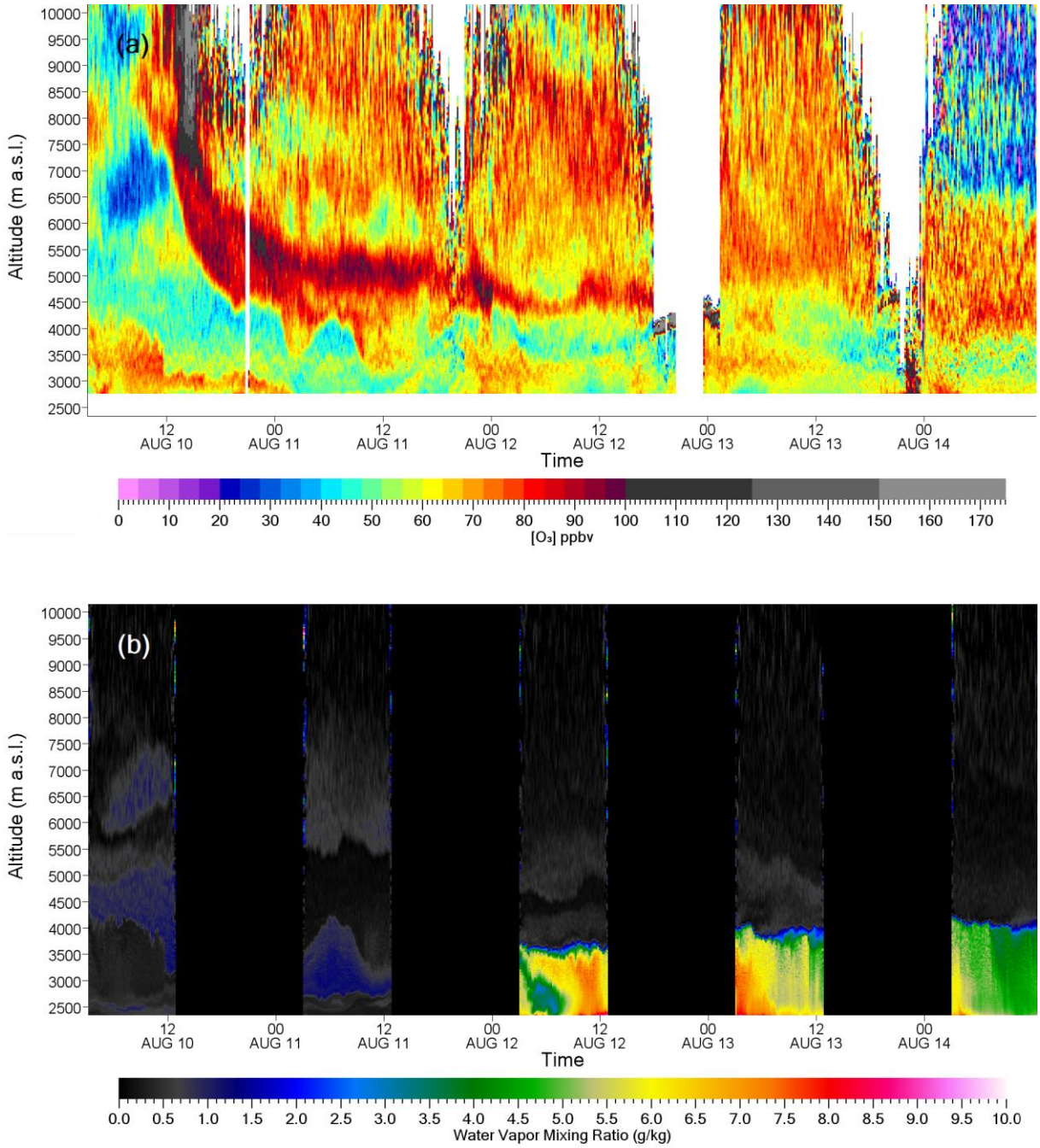
(a)
Altitude (m a.s.l.)
10000
9500
9000
8500
8000
7500
7000
6500
6000
5500
5000
4500
4000
3500
3000
2500
12 AUG 10
00 AUG 11
12 AUG 11
00 AUG 12
12 AUG 12
00 AUG 13
12 AUG 13
00 AUG 14
Time
0 10 20 30 40 50 60 70 80 90 100 110 120 130 140 150 160 170
[O3] ppbv
(b)
Altitude (m a.s.l.)
Time
0.0 0.5 1.0 1.5 2.0 2.5 3.0 3.5 4.0 4.5 5.0 5.5 6.0 6.5 7.0 7.5 8.0 8.5 9.0 9.5 10.0
Water Vapor Mixing Ratio (g/kg)

Fig. 9

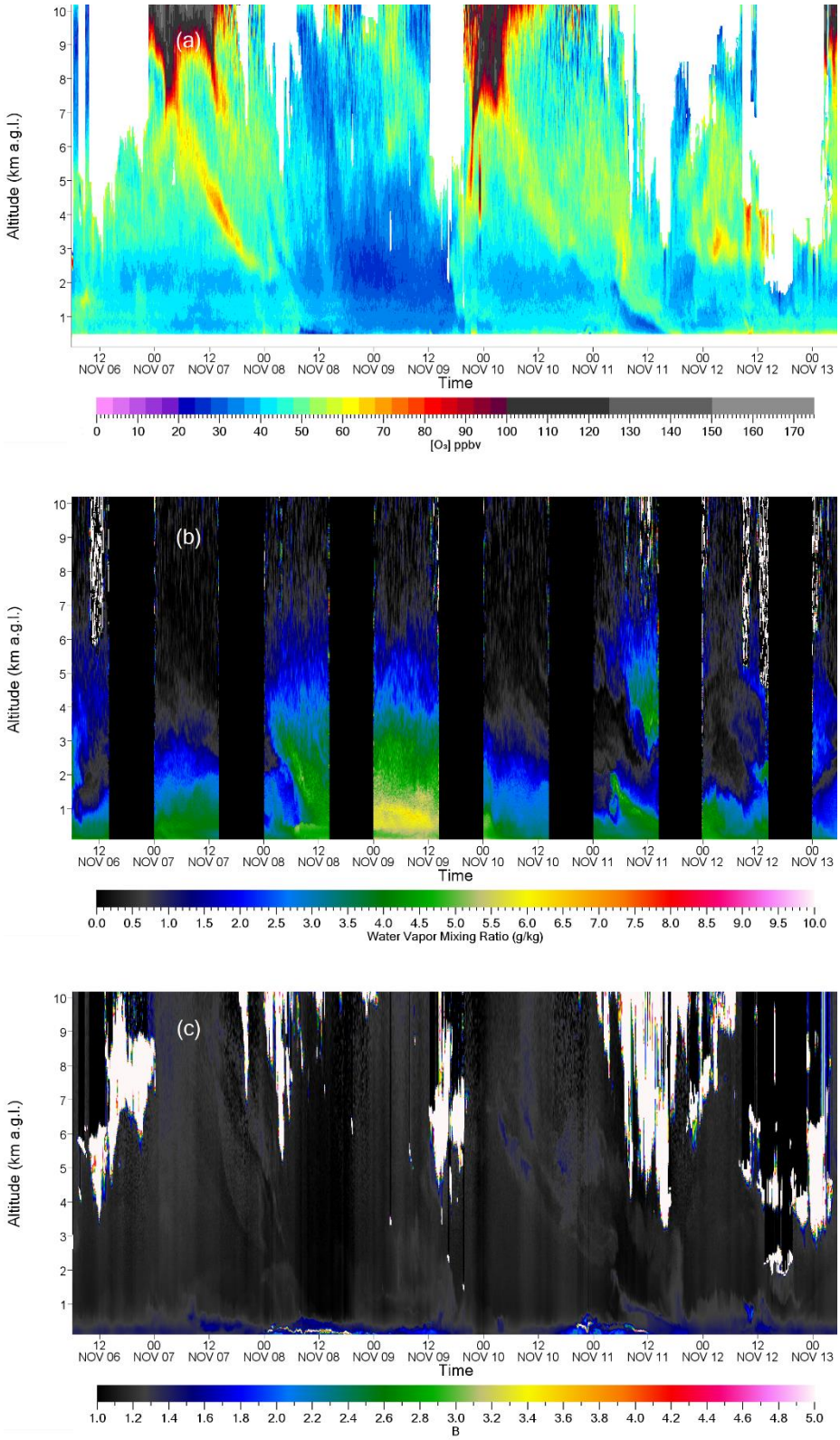
(a)
Altitude (km a.g.l.)
Time
[O3] ppbv
(b)
Water Vapor Mixing Ratio (g/kg)
(c)
B

1 Fig. 10

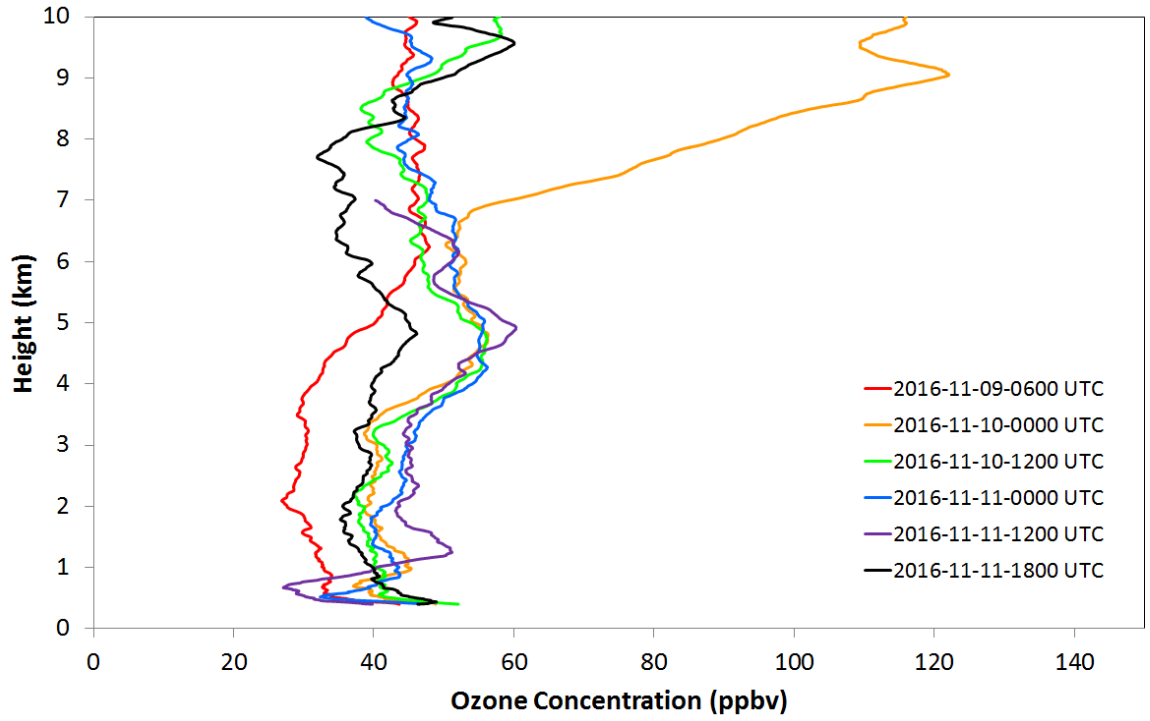
Height (km)
Ozone Concentration (ppbv)
0
1
2
3
4
5
6
7
8
9
10
0
20
40
60
80
100
120
140
2016-11-09-0600 UTC
2016-11-10-0000 UTC
2016-11-10-1200 UTC
2016-11-11-0000 UTC
2016-11-11-1200 UTC
2016-11-11-1800 UTC

2

3

Fig. 11

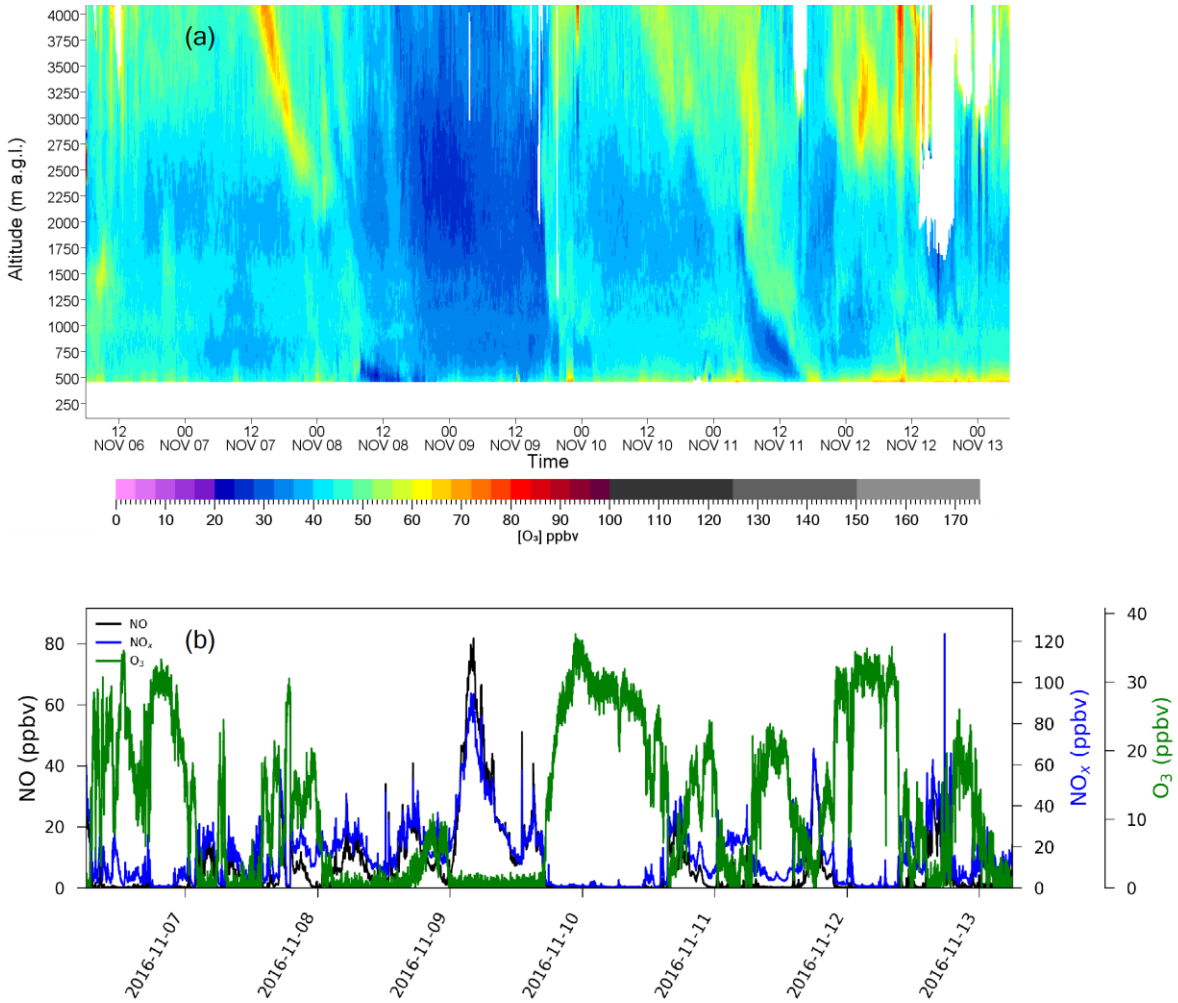
(a)
Altitude (m a.g.l.)
4000
3750
3500
3250
3000
2750
2500
2250
2000
1750
1500
1250
1000
750
500
250
12 NOV 06
00 NOV 07
12 NOV 07
00 NOV 08
12 NOV 08
00 NOV 09
12 NOV 09
00 NOV 10
12 NOV 10
00 NOV 11
12 NOV 11
00 NOV 12
12 NOV 12
00 NOV 13
Time
0 10 20 30 40 50 60 70 80 90 100 110 120 130 140 150 160 170
[O3] ppbv
(b)
NO
NOx
O3
NO (ppbv)
NOx (ppbv)
O3 (ppbv)
2016-11-07
2016-11-08
2016-11-09
2016-11-10
2016-11-11
2016-11-12
2016-11-13

1 Fig. 12

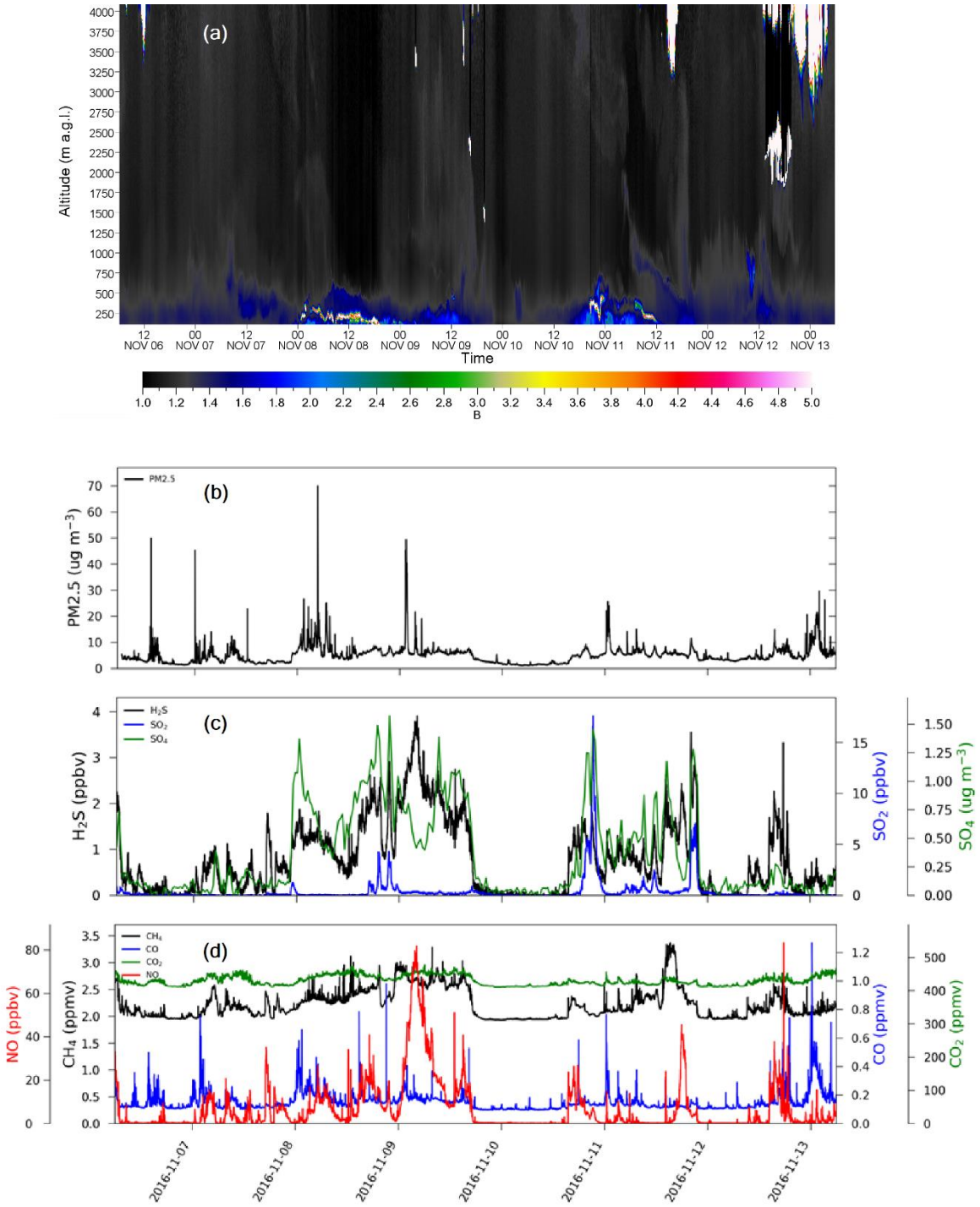
(a)
Altitude (m a.g.l.)
Time
B
(b)
PM2.5
PM2.5 (ug m⁻³)
(c)
H₂S
SO₂
SO₄
H₂S (ppbv)
SO₂ (ppbv)
SO₄ (ug m⁻³)
(d)
CH₄
CO
CO₂
NO
NO (ppbv)
CH₄ (ppmv)
CO (ppmv)
CO₂ (ppmv)
2016-11-07
2016-11-08
2016-11-09
2016-11-10
2016-11-11
2016-11-12
2016-11-13

2

3

Fig. 13

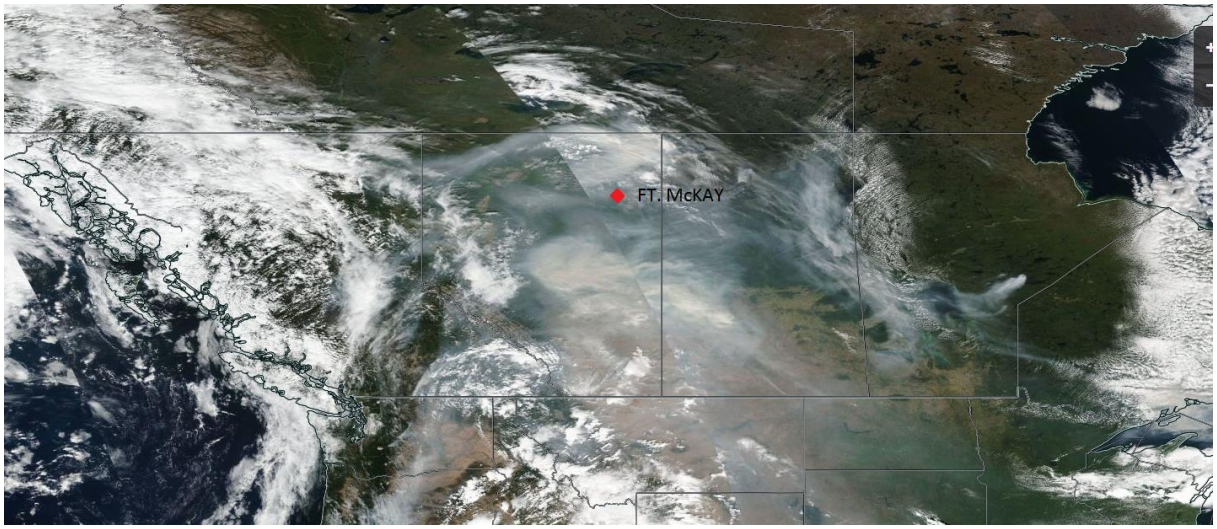

1 Fig. 14

2

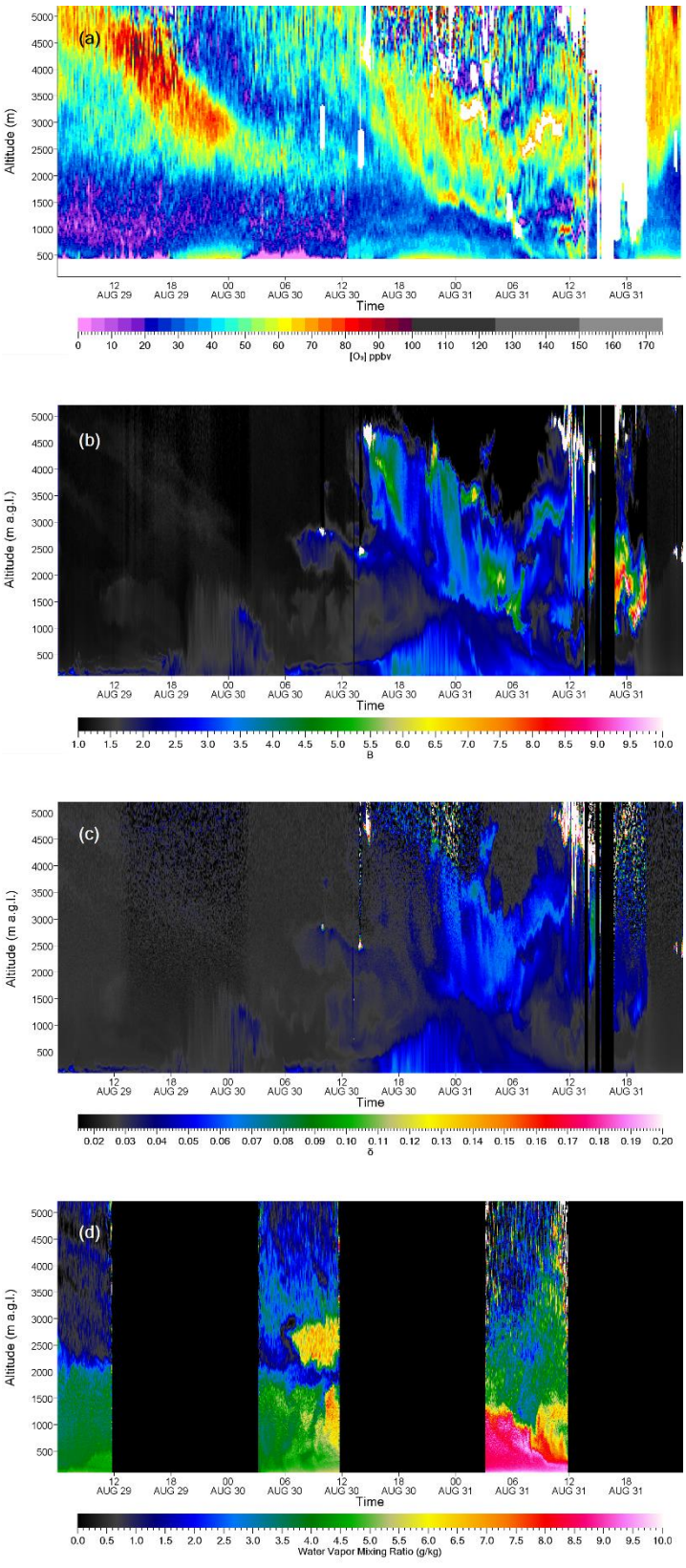
(a)
Altitude (m)
Time
[O3] ppbv
(b)
Altitude (m a.g.l.)
Time
B
(c)
Altitude (m a.g.l.)
Time
δ
(d)
Altitude (m a.g.l.)
Time
Water Vapor Mixing Ratio (g/kg)

3

4

1 Fig. 15

2

3

4

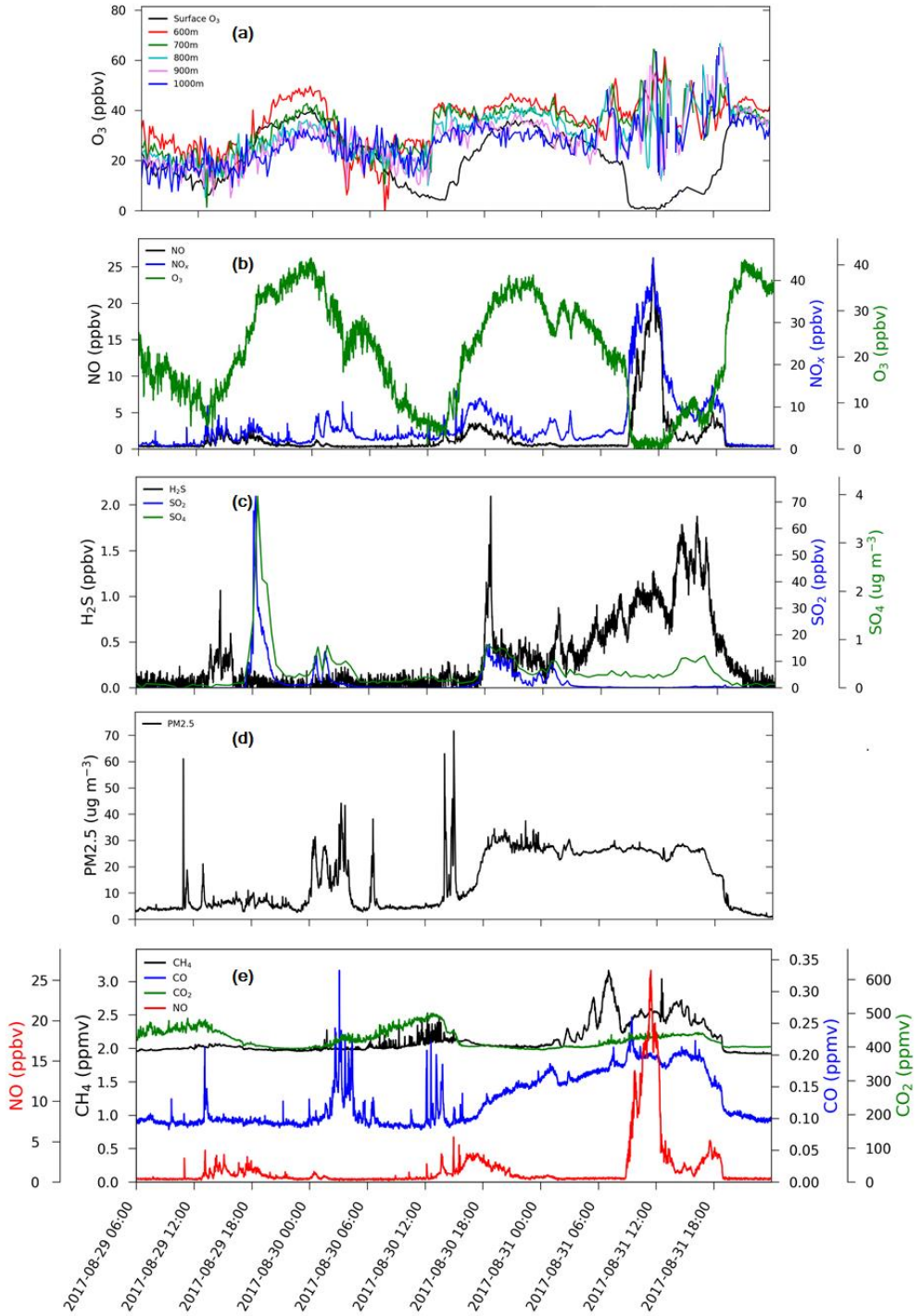
(a)
Surface O3
600m
700m
800m
900m
1000m
O3 (ppbv)
(b)
NO
NOx
O3
NO (ppbv)
NOx (ppbv)
O3 (ppbv)
(c)
H2S
SO2
SO4
H2S (ppbv)
SO2 (ppbv)
SO4 (ug m−3)
(d)
PM2.5
PM2.5 (ug m−3)
(e)
CH4
CO
CO2
NO
NO (ppbv)
CH4 (ppmv)
CO (ppmv)
CO2 (ppmv)
2017-08-29 06:00
2017-08-29 12:00
2017-08-29 18:00
2017-08-30 00:00
2017-08-30 06:00
2017-08-30 12:00
2017-08-30 18:00
2017-08-31 00:00
2017-08-31 06:00
2017-08-31 12:00
2017-08-31 18:00

5

~~Fig. 17~~

Fig 16

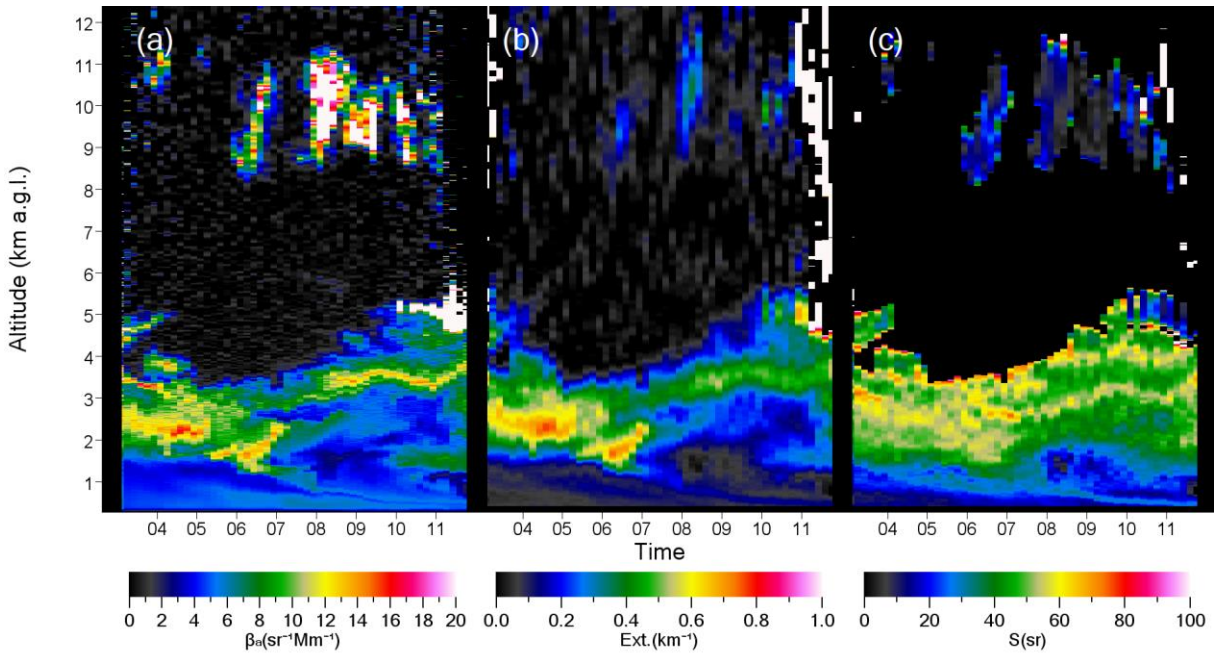
(a)
(b)
(c)
Altitude (km a.g.l.)
12
11
10
9
8
7
6
5
4
3
2
1
04 05 06 07 08 09 10 11
Time
0 2 4 6 8 10 12 14 16 18 20
βe(sr⁻¹Mm⁻¹)
0.0 0.2 0.4 0.6 0.8 1.0
Ext.(km⁻¹)
0 20 40 60 80 100
S(sr)

Fig. 1~~7~~8

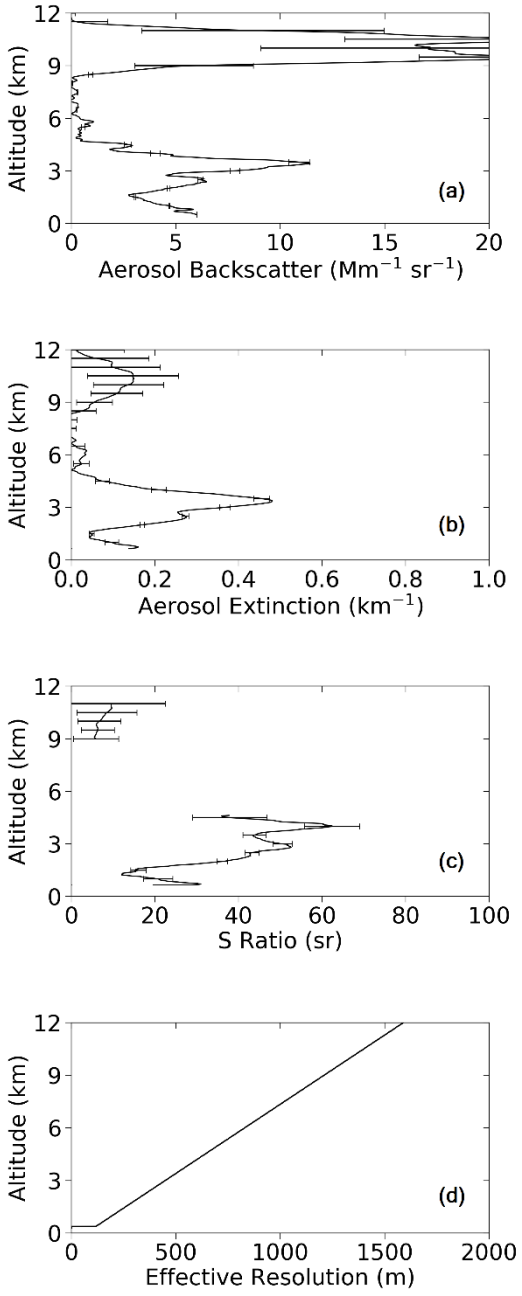
Altitude (km)
Aerosol Backscatter (Mm^{-1} sr^{-1})
(a)
Aerosol Extinction (km^{-1})
(b)
S Ratio (sr)
(c)
Effective Resolution (m)
(d)

Fig. 1~~8~~9

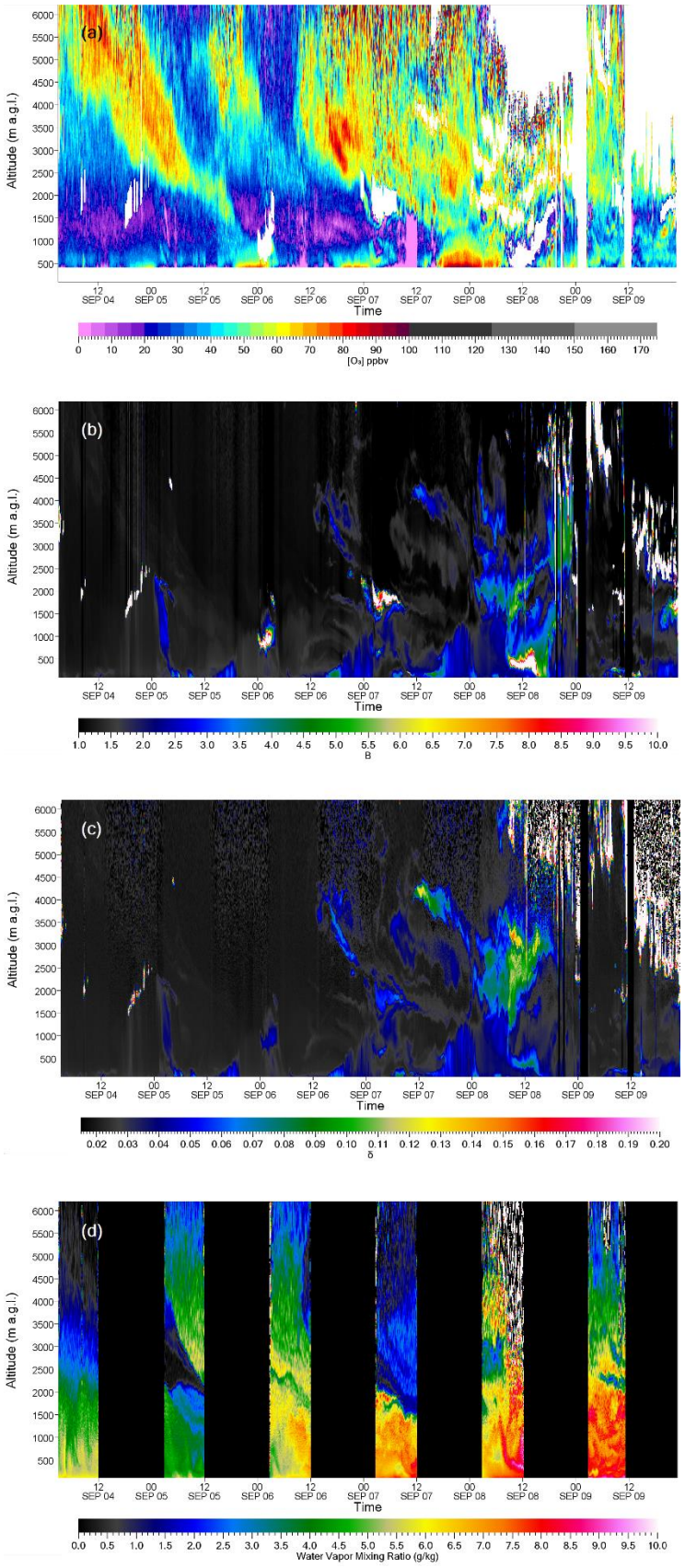
(a)
Altitude (m a.g.l.)
Time
[O3] ppbv
(b)
Altitude (m a.g.l.)
Time
B
(c)
Altitude (m a.g.l.)
Time
δ
(d)
Altitude (m a.g.l.)
Time
Water Vapor Mixing Ratio (g/kg)

Fig. 19~~20~~

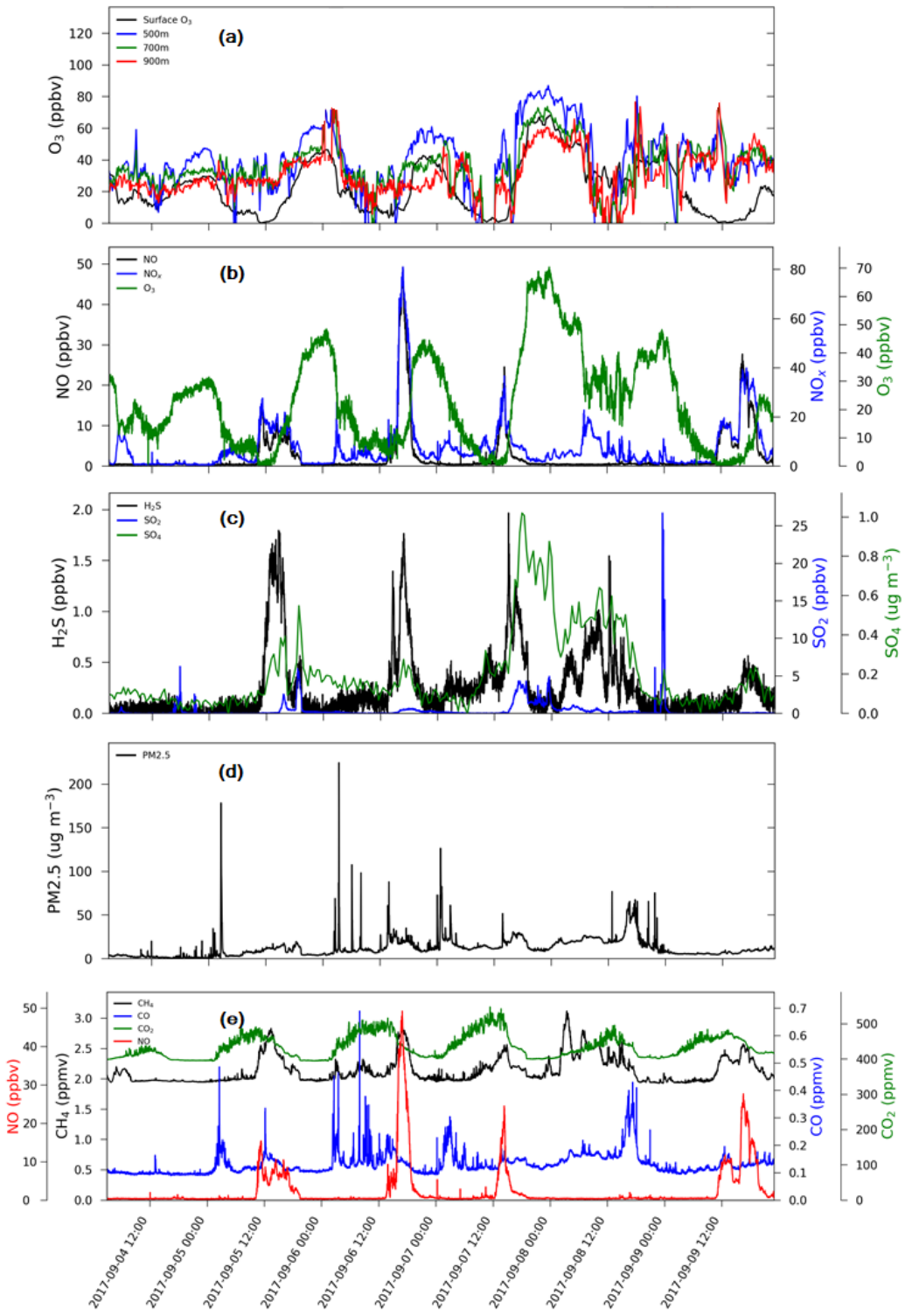
(a)
Surface O3
500m
700m
900m
O3 (ppbv)
(b)
NO
NOx
O3
NO (ppbv)
NOx (ppbv)
O3 (ppbv)
(c)
H2S
SO2
SO4
H2S (ppbv)
SO2 (ppbv)
SO4 (ug m−3)
(d)
PM2.5
PM2.5 (ug m−3)
(e)
CH4
CO
CO2
NO
NO (ppbv)
CH4 (ppmv)
CO (ppmv)
CO2 (ppmv)
2017-09-04 12:00
2017-09-05 00:00
2017-09-05 12:00
2017-09-06 00:00
2017-09-06 12:00
2017-09-07 00:00
2017-09-07 12:00
2017-09-08 00:00
2017-09-08 12:00
2017-09-09 00:00
2017-09-09 12:00

Fig. 2~~01~~

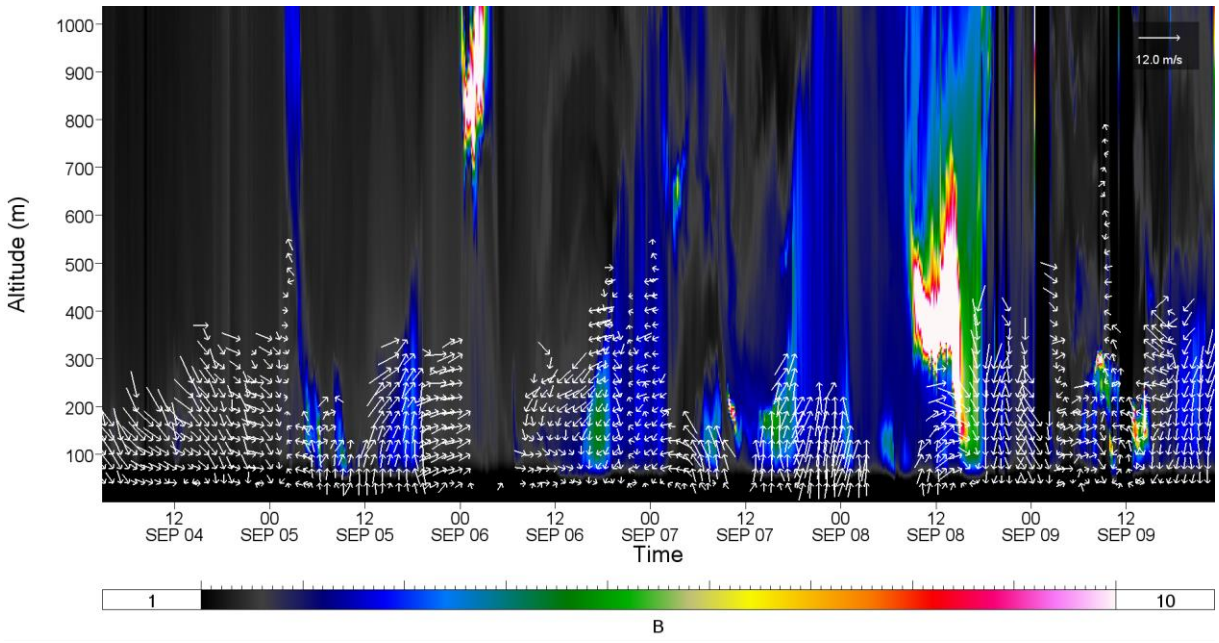
Altitude (m)
1000
900
800
700
600
500
400
300
200
100
12.0 m/s
12 SEP 04
00 SEP 05
12 SEP 05
00 SEP 06
12 SEP 06
00 SEP 07
12 SEP 07
00 SEP 08
12 SEP 08
00 SEP 09
12 SEP 09
Time
1
10
B

Fig. 2~~12~~

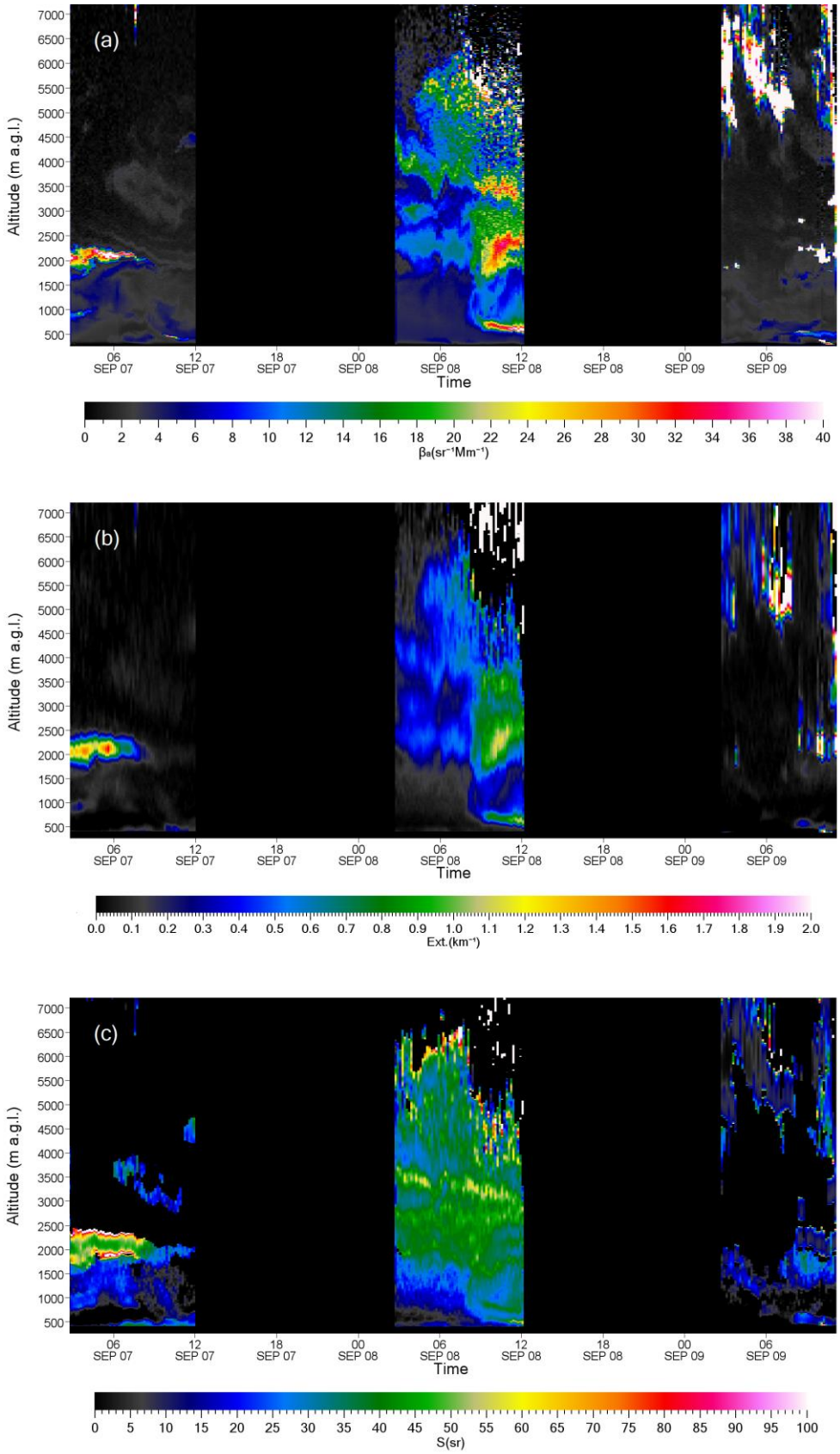
(a)
Altitude (m a.g.l.)
7000
6500
6000
5500
5000
4500
4000
3500
3000
2500
2000
1500
1000
500
06 SEP 07
12 SEP 07
18 SEP 07
00 SEP 08
06 SEP 08
12 SEP 08
18 SEP 08
00 SEP 09
06 SEP 09
Time
0 2 4 6 8 10 12 14 16 18 20 22 24 26 28 30 32 34 36 38 40
βa(sr⁻¹Mm⁻¹)
(b)
Altitude (m a.g.l.)
Time
0.0 0.1 0.2 0.3 0.4 0.5 0.6 0.7 0.8 0.9 1.0 1.1 1.2 1.3 1.4 1.5 1.6 1.7 1.8 1.9 2.0
Ext.(km⁻¹)
(c)
Altitude (m a.g.l.)
Time
0 5 10 15 20 25 30 35 40 45 50 55 60 65 70 75 80 85 90 95 100
S(sr)

Fig. 2~~3~~

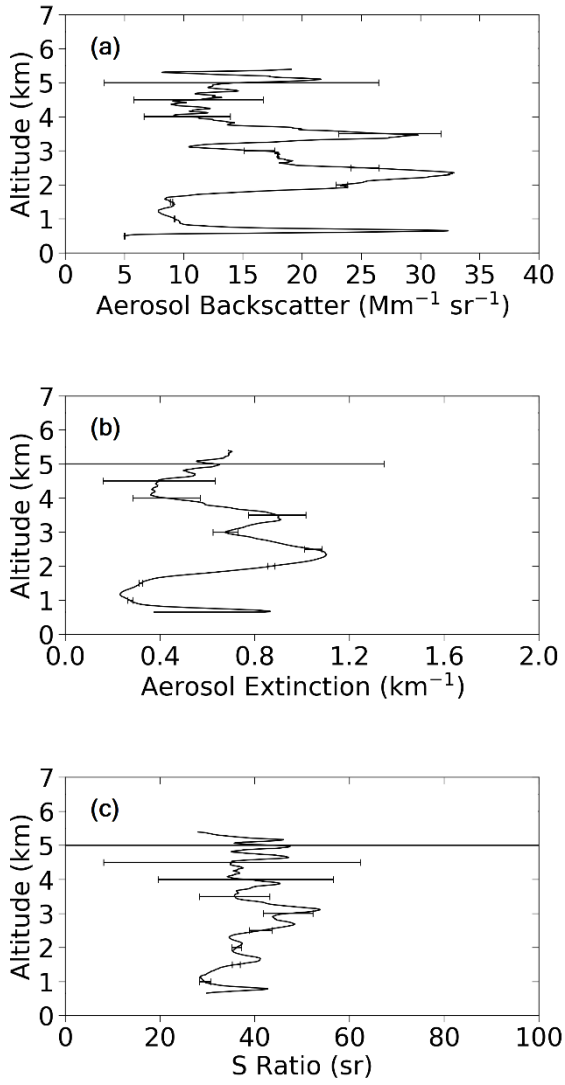
(a)
Altitude (km)
Aerosol Backscatter (Mm^{-1} sr^{-1})
(b)
Altitude (km)
Aerosol Extinction (km^{-1})
(c)
Altitude (km)
S Ratio (sr)

Fig. 2~~3~~4

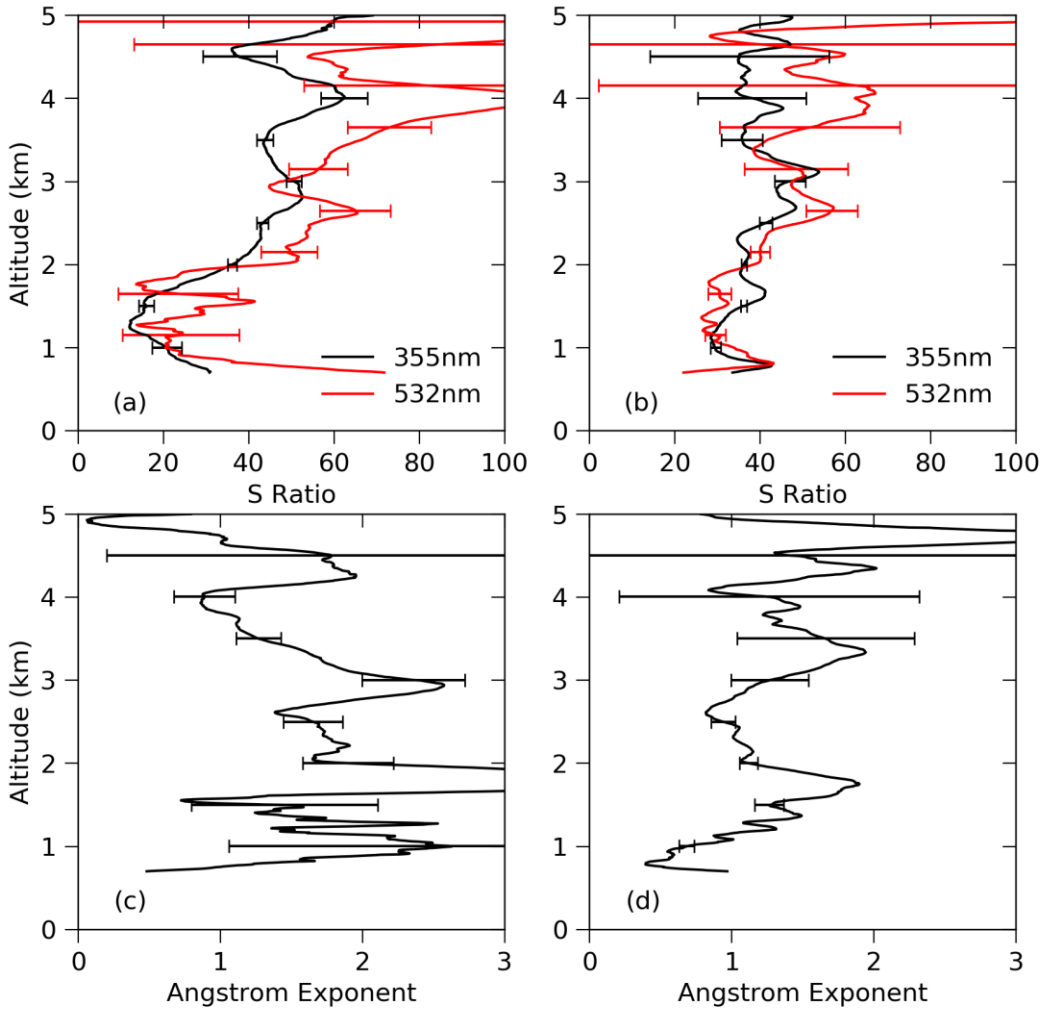

Review of Manuscript amt-2018-108
Observations and analysis of UTLS aerosol detected over northern France

Incorrect manuscript title, see title below

A fully autonomous ozone, aerosol and night time water vapor LIDAR: a synergistic approach to profiling the atmosphere in the Canadian oil sands region

by K. Strawbridge et al.
June 22, 2018
The authors would like to thank the reviewer for their comments and suggestions.

The paper describes a very promising lidar trailer featuring autonomous measurements of the three most important species that can be measured with lidar. The capability of the system is well documented and demonstrates the high value of simultaneous and continuous lidar measurements of several species. I recommend publication after modifications based on the following comments:

P. 2, line 4: Add a statement on the level of dryness found in intrusions.
Statement added giving measured values.

P. 3, line 8: I am not sure if these two references are suitable for documenting ozone production in biomass-burning plumes. This process has been verified at lower latitudes, but there is doubt in ozone formation at high latitudes. See also my remarks below.
The reference of Aggarwal et al. was chosen because it is another recent documented case of ozone production in a biomass-burning plume in the region.
Also added another reference

P. 3, line 10: The selection of literature in some way seems to reflect a historic sequence. Thus, I suggest to cite Stohl and Trickl, J. Geophys. Res. 104 (1999), 30445-30462, instead of (Trickl et al., 2015). Another nice paper is J. Geophys. Res. 117 (2012), D18305, doi:10.1029/2012JD017695.
Perhaps the review means Trickl et al., 2014. Trickl et al., 2015 is the forest fire reference and Trickl et al., 2014 is the STT reference.
Trickl reference removed and replaced with Stohl and Trickl reference.

P. 3, line 14: Please, add “and water vapor”.
Added “and water vapor”

P. 3, lines 27-28: “aerosol processes” are (e.g.) particle growth, particle evaporation, chemical transformation, heterogeneous chemistry. I doubt that lidar measurements can yield insight into these processes. Lidar measurements can yield hints on transport or optical properties. Please, rephrase!
Sentenced rephrased, removed “aerosol processes”.

P. 4, line 4: Water vapour is the primary greenhouse gas, responsible for 2/3 of the greenhouse effect. Please, change phrase to “Also, as the primary greenhouse gas”.
Phrase changed.

P. 4, line 7: You could add a sentence concerning the extreme spatial and temporal variability of

water vapour (Vogelmann et al., Atmos. Chem. Phys. 14 (2015), 3135-3148). This is a great problem for trend studies, but a strong motivation for lidar measurements because of the good spatial and temporal resolution.
Sentence added and Vogelmann et al., reference also added.

P. 4, line 15: "Garmisch-Partenkirchen/Zugspitze"? In principle, "Garmisch-Partenkirchen" would be enough since the Zugspitze mountain belongs to that town.
Zugspitze removed.

P. 4, line 17: Replace "However, all of" by "Several of": OHP is not a high-mountain site at all, and in Garmisch-Partenkirchen most lidar systems are not located at high altitude. I think all three species are also measured at Table Mountain.
Replaced "However, all" with "Several".

P. 5, lines 1-4: There are several lidar networks such as the lidar team of NDACC, EARLINET, the East Asian lidar network and others. References: For NDACC: web site; for EARLINET Papayannis et al., J. Geophys. Res. 113 (2008), D10204; doi: 10.1029/2007JD009028, Pappalardo et al., Atmos. Chem. Phys. 13 (2013), 4429-4450.
Added references

P. 5, line 10: AB presumably means "Alberta". There may be readers who do not know this.
Changed "AB" to "Alberta"

P. 5, lines 16-17: What does CAMI and the text in brackets mean?
Fixed text

P. 7: In an autonomous system automatic data evaluation is an important issue. I did not find much on this topic, in particular on the quality of automatic aerosol corrections. This is a rather demanding procedure that usually introduces additional uncertainty. Several methods exist and are discussed in (Eisele and Trickl, Appl. Opt. **44** (2005), 2638-2651).
text added to the conclusions and future work to address this

P. 7, line 10: Add reference (e.g., Leblanc et al., Atmos. Meas. Tech. 9 (2016), 4029-4049).
Reference added.

P. 7, line 15: "the addition of just a few optics"; one could mention the small addition space requirement. A DIAL would require much more space and is more complex, but would allow daytime measurements.
Added text and reference to Figure

P. 7, line 24. "absorption" is perhaps not fully adequate. Raman scattering is a two-photon scattering process. An "intermediate electronic state" may exist or not. In general non-resonant scattering is considered. Please, rephrase!
Sentence was rewritten.

P. 9, line 12: Unfortunately, somebody in the remote past who obviously had no idea about the benefits of the ideal gas law introduced g/kg for H_2O instead of the volume mixing ratio.

Generations of H_2O researchers then followed this example. In atmospheric sciences usually the volume mixing ratio is used and I recommend the authors to join the community in the future.
P. 10, line 19: Please, add statement about the section where the figure is described.
Statement added

P. 11, line 6: What kind of optic?
Added more to the description and provided manufacturer

P. 22: Computer cards pick up noise from the computer. How clean is the signal?
Assuming this comment is for P. 11, line 22: I added a sentence

P. 11, line 29-30: Only one of the two 45º optics is explained!
Added sentence.

P. 12, line 31: 45 mJ: 266 nm?
Added 266 nm to sentence.

P. 13, line 2: 20 %????
Changed to 20%

P. 13, line 17: The events are not mixed! Change to "in long term events" ("in long-term events").
Added dash

P. 13, line 23: The two color-coded plots?
Added "color-coded"

P. 13, line 25;: "mixes down": There is not much mixing in the free troposphere. "descends" is more adequate. See also Fig. 10.
Changed "mixes down" to "descends" here and in Fig. 10

P. 14, line 9: Explain "boxcar smoothing" (at least add a reference)
Added text

P. 14, line 24-25: Confusing sentence! If you mean "all corrections but" (comma removed): the cross sections are no correction!
Changed "corrections" to "terms"

P. 15, line 31: "observing the impact of many atmospheric processes" (see above).
changed

P. 16, lines 5.6: This is a highly remarkable statement and deserved a few more words! At lower latitudes (Granados-Munoz, Leblanc, Atmos. Chem. Phys. 16 (2016), 9299-9319) also high fractions were reported for winter, but not for summer. It seems that STT is more important (at least in mid-latitudes) that previously thought, as indicated by Trickl et al. (Atmos. Chem. Phys. 10 (2010), 499-524).

Statement removed - given this paper is on only one year of data, the authors are uncomfortable making statements about seasonal characteristics of STT events

P. 16, line 15: How dry? 50-100 ppm would be indicative for UTLS air, 4-5 ppm for free stratospheric air (e.g., Hurst et al., J. Geophys. Res. 116 (2011), D02306, doi: 10.1029/2010JD015065). For consistency you should convert 50-100 ppb and 4-5 ppb to g/kg.
Included actual value of "dry air"

P. 16, line 23: Please specify where 120 ppb is reached (not in the intrusion peaks!).
Time is now specified

P. 17, line 19: "well documented": See above (P. 3)! How do you know?
Removed statement

P. 17, line 25: The air seems to be dry: Can you exclude an intrusion? See (Trickl et al., 2015) for examples. Did you calculate trajectories?
Added some text to link enhanced ozone with high aerosol and depolarization ratio. Also added a reference.

P. 17, lines 29-30: On what basis do you hypothesize?
See above.

P. 18, line 14: Please, define S!
S ratio is the extinction-to-backscatter ratio – added dashes

P. 18, line 30: The determination of lidar ratios is highly uncertain since the calculation of small extinction coefficients is based on derivate formation. A few error bars in the lidar-ratio plots would be helpful.
Error bars added

P. 19, line 1: "in this case"?
Added "in"

P. 19, line 10 ": "is due to the forest fire activity": Please, provide evidence. The air seems to be rather dry which could, again, suggest STT. Did you calculate trajectories?
See P17 line 25 above

P. 19, li ne 20.21: levels are, level is?
Changed "is" to "are"

P. 20, line 11-13: Error bars are missing (see above); add a few.
Error bars added

P. 21, line 32: The "valuable dataset" was already emphasized. Maybe you could write "provide further value".

Changed text

Figures:
The symbols are frequently rather small. The colour coding is no clear. Black looks like absence of data. I suggest to use a brighter grey to achieve more contrast. At least statements about the concentrations in the "black" altitude range would be helpful. Finally: Add numbers to the colour scales!
Plots have been redone

Figs. 2, 3, others: Add something like "The abbreviations are explained in a separate box in the plot".
Text added to figure caption

Fig. 11, 12, 15, 20: The colours are hard to distinguish in the legend (the text is also small)
Changed plots

Fig. 5: Please, specify the shift of the local time with respect to UTC.
Test added

Style:
P. 1, line 29: "we added" instead of "we have added"?
Removed "have"

P. 3, line 20: "travel over"?
Added "over"

P. 3, line 27: "therefore" / ",therefore,": There is an obvious trend in the literature for less punctuation. Within the papers I have reviewed this one is record setting in omitting commas and hyphens.
Added comma

P. 4, line 24: "to simultaneously measure" (and other examples in the paper, e.g., P. 5 line 6, P. 14, line 3): split infinitive!
corrected

P. 12, line 9: Stanford
Corrected spelling

P. 12, line 13: Add a comma between "week" and "except" for clarity.
Added comma

P. 13, line 18: signal to noise ratio (signal-to-noise ratio)
Added dashes

P. 21, line 16: "The three-LIDAR system" would be clearer

Added dash

In the AMT-2018-108 manuscript titled "A fully autonomous ozone, aerosol and night time water vapor LIDAR: a synergistic approach to profiling the atmosphere in the Canadian oil sands region" Strawbridge et al. describe the development and application of the AMOLITE autonomous lidar for profiling of ozone, aerosol and water vapor. In the first part of the paper, the authors discuss the hardware upgrades to an existing Environment Canada autonomous aerosol lidar to enable unattended ozone and water profiling and they provide a detailed account of their efforts to validate the ozone lidar component of AMOLITE. In the second part of the paper, the authors show three multi-day measurement examples from the one-and-a-half-year (and counting) deployment of AMOLITE in the Canadian oil sands region in northeastern Alberta. They use the AMOLITE profile measurements together with in situ chemistry and radar-RASS wind profiler observations to characterize the transport patterns and source regions of atmospheric pollutants observed in the oil sands region.

While unattended aerosol and Raman water vapor lidars have been successfully operated before, the autonomous ozone lidar component of AMOLITE is the first of its kind. The authors have used a tried-and-true approach for the ozone lidar transmitter (Raman shifting of quadrupled NdYAG laser output in a gas cell), then hardened the instrument, built in redundancy, and designed a sophisticated environmental control system. The fact that AMOLITE has been operating continuously for over a year in the harsh environment of northern Alberta is remarkable. This instrument represents a breakthrough in our ability to monitor over long time periods the vertical structure and transport processes of ozone in the troposphere. The water vapor and aerosol profiling capabilities provide important additional information that allows fingerprinting of the air masses and identification of ozone source regions.

The topic of the paper fits well within the scope of AMT. The conclusions presented in the manuscript are supported by the data and figures. While the manuscript contains a rather large number of figures I find them all (except for one) necessary to showcase the synergistic advantages of combining long-term profile and in situ observations. Certain parts of the paper have deficiencies and need a significant overhaul (see major comments below). Therefore, **I recommend publication after major revisions.**

The authors would like to thank the reviewer for their comments and suggestions.

Every plot was re-done for the paper which was a tremendous amount of work that required considerable coding as the plotting software is a custom package.

Major comments

1) The section on the ozone DIAL technique (2.1) does not cover all the important aspects of the ozone DIAL retrieval and contains several factual errors. The interfering trace gas correction term needs to be included in equation 1 (page 5): $N(z) = \ldots + 2 \square\square(z) + 2 \square_I \square\square_i n_i(z)]$, with $\square\square_I$ = differential cross section of interfering trace gas and $n_i(z)$ = number density profile of interfering trace gas. Equation 2 (page 5) is incorrect. It should read: $d/dz \{\ln [B_{on}(z)/B_{off}(z)]\} = d/dz \{\ln[(1 + S\ldots)/(1+ S\ldots)]\}$. The term 'backscatter ratio" is used for the B_{on}/B_{off} ratio and the aerosol to molecular backscatter ratio S as defined by Kovalev et al. The authors point out that the 'on', 'off', and 'reference' wavelengths are 287, 299, and 355 nm, respectively. However, the O_3 lidar wavelengths have only been mentioned in the abstract at this point and are not introduced in the main text until sections 3.2 and 3.3. The last sentence in section 2.1 describes how the ozone lidar raw data are smoothed and how the derivative of the log signal ratios are computed. This is specific to the AMOLITE ozone

retrieval algorithm and does not belong in the general ozone DIAL technique section. I suggest to merge this sentence and the statement about 'on', 'off', and 'reference' wavelengths with section 3.5, rename that section to "AMOLITE Ozone DIAL Algorithm and its Validation", and swap positions with the current section 3.4. In the current section 3.5 (AMOLITE Algorithm Validation), the authors mention that they selectively tested individual steps of the ozone DIAL algorithm, including deadtime and background correction and Rayleigh extinction correction. These different steps of the retrieval need to be first introduced. Indeed, the reviewer is correct – the equations have been changed. I have also moved the last paragraph from Section 2.1 to Section 3.5 and re-ordered it to become Section 3.4 as suggested. More details have now been provided on the various corrections applied to the retrieval

2) The section on the water vapor Raman retrieval technique (2.2) can be shortened, especially the number of equations. The authors describe in rather great detail the derivation of the equations underpinning the water vapor Raman retrieval. I suggest to just list equations 7-9. Section 2.2 was shortened to only include equations 7-9 which are now of course renumbered.

3) In the AMOLITE Instrument Validation and Calibration section (3.4), the authors describe the rigorous validation of the ozone DIAL part of AMOLITE during the SCOOP campaign. Did the authors also validate the Raman water vapor channel in a similar manner? The calibration of the Raman water vapor channel is referenced – we used the sonde data during SCOOP - added text

4) It is unclear to me whether the authors apply differential aerosol backscatter and extinction corrections. Both correction terms are listed in equation (1) in section 2.1, but no mention of the aerosol correction terms is made in the algorithm validation section (3.5). Aerosol correction is important, especially in or near industrial or fire plumes that seem to regularly impact the Oski-otin site, because of the strong aerosol gradients that can be associated with these plumes. An example for this is a piece of a fire plume observed with AMOLITE on 31 August 2017 around 2000 UTC between about 1000 and 2000 m agl (Fig. 14b), with sharp aerosol gradients near the bottom and top of the plume. The coincident ozone measurements (Fig. 14a) show very high ozone concentration near the bottom of the plume and very low ozone concentrations near the top of the plume. This is consistent with O_3 biases due to differential aerosol effects (the authors allude to this in section 4.1, page 17, lines 1-3). Similar high/low O_3 couplets can be found on 30 August near 2500 - 3000 m agl again near aerosol blobs with sharp gradients at their boundaries. The authors need to clarify whether or not they applied aerosol correction and how they did or how they plan to implement the corrections, including aerosol backscatter retrieval at 355 nm, and choice of Angstroem coefficients for both aerosol backscatter and extinction.

Text has now been added to section 3.4 and plots redone

5) For the same reasons as pointed out under 4), biases in ozone lidar measurements can also occur near the bases of clouds when cloud returns are not properly filter out. This appears to be the case on 12 November 2016 around 1500 UTC at about 2000 m agl. Did the authors filter out cloud returns and, if so, which approach did they use? Figures redone – the ozone plots were cloud-screened using the aerosol LIDAR6) The CAM1 in situ instruments at the Oski-otin site occasionally observe large SO_2 concentrations (up to 70 ppbv on 8/29/17, 27 ppbv on 9/9/17, and 18 ppbv on 11/11/16), presumably when the industrial plumes get advected to the site. Did the authors make an attempt to correct for SO_2 interference in their O_3 lidar analysis? Using the Brion et al. (1992-1998) O_3 and Vandaele, Hermans, and Fally (2009) SO_2 absorption cross section data, I get an interference term of approximately 36%*SO_2 concentration for the 287.2 / 299.14 wavelength pair, which would result in O_3 mixing ratio overestimations of about 25, 10, and

6 ppbv for the above SO_2 values. With only surface SO_2 measurements available, it is difficult to estimate SO_2 concentrations at the O_3 lidar altitudes (>= 500 m agl). Perhaps one could use mixing heights determined from the aerosol lidar observations to get a rough idea what the SO_2 concentrations might be at the lower O_3 lidar altitudes. Most of the time, the SO_2 concentrations are small enough, so that the interference term is insignificant. However, in the cases of concentrated SO_2 plumes impacting the Oski-otin site, the authors need to provide an estimate of the error in their O_3 lidar measurement due to SO_2 interference.-Text was now added – data was screened out of the plots – as the reviewer noted it is very difficult to estimate SO_2 concentrations aloft – plots were redone

Minor comments

Page 2, lines 7-9: "The advantage of nearly …."

I suggest to leave this sentence out. It sounds more like a statement one would find in a conference abstract. Removed this sentence as requested

Page 3, line 13

"… atmospheric mixing processes" or "… atmospheric mixing and **exchange** processes"?

Added "exchange"

Page 4, line 4-5: 'Dynamics' is a bit misleading here. How about "… advance our understanding of **the trace gas distribution in the lower atmosphere**…"?

Changed wording to above

Page 4, lines 23-24: "The first AMOLITE ozone and water vapor profiles at the Oski-otin ground site in Fort McKay, AB were acquired on 3 November 2016."

Changed to wording above

**** The page and line numbers going forward from here do not match the page and line numbers on the PDF file in AMTD. The other reviewer page and line numbers matched so not sure what happened but it has made it more difficult to reference the corrections******

Page4, lines 31-32: Reference for CAM1 measurements is missing. Also, state briefly which gases and particulates are measured by the CAM1 instruments.

Changed text as no reference available yet for CAM1 – the list of observables is quite extensive, only a small number of them are used in this manuscript

Page 5, line 14: "**The AMOLITE instrument** uses three different …"

Changed text to above

Page 5, line 15: Aerosol profile measurements at the third wavelength (1064 nm) are not shown in this paper. What is the reason for that?

Text added in Section 3.2

Page 5, line 17: "… to measure t**he** water vapor profile."

Added "the"

Page 5, line 19-20: "… used in AMOLITE"

Changed "employed" to "used"

Page 5, line 25: "… to have a **sufficiently** large difference … Added "sufficiently:

Page 6, line 2: "… differential ozone absorption **cross section**, … Added "cross section"

Page 6, line 3: "… the total **two-way extinction coefficient** differential" Changed wording

Page 6, lines 4-9: "Solving for the component …" Awkward and confusing sentence. Please restate.

Changed wording

Page 6, line 14: "… Savitzky-Golay convolution **to compute the derivative with respect to altitude of the signal ratio and B_{on}/B_{off}."** Move to new section 3.4 as suggested above. Added text
Page 8, lines 9-13: The explanation of the symbol S in equation 9 is unclear.

Page 8, line 23: "… the trailer needed to **have a** slightly larger…"
Changed wording
Page 9, line 14: "… between 6000 and 24000 BTU of cooling with external temperatures as low as -40C …" 6000 and 24000 BTU of **heating**? Perhaps list the full external temperature range and state the heating and cooling capacities?
Added text
Page 9, line 20: "…improvements of the trailer infrastructure …"
Deleted text
Page 10, line 5: "… are triple-coated … 50 mmm optic**s** …"
Removed "a"
Page 11, line 16: "… to compare **AMOLITE** ozone profiles **to** other LIDAR instruments …"
Replaced "LIDAR" with "AMOLITE"
Page 11, line 21: Leblanc et al., 2016b is missing in the reference section.
Changed "b" to "a" and added correct reference
Page 11, lines 27: "… measurements **at night** will reach a range of over 10 km **agl** and dip to 7 km **agl around midday when solar background is high**"
Changed wording
Page 11, line 29: "… staying within approximately 10% of the ozone sonde values …" Differences are up to 20% at several altitudes and approx. 50% at 7.5 km MSL in Fig. 5b. Please reword this statement.
Added a few sentences to clarify
Page 12, line 3-4: "This **is** shown in Figure 6 …"
Changed "can be" to "is"
Page 12, line 11 "… throughout the **diurnal cycle** …"
Changed "daylight" to "diurnal"
Page 12, lines 24-25: "**The water vapor measurements below 4 km on 10 August show** very dry air …"
Changed wording
Page 13, line 7: "… both the simulate**d** LIDAR data and …"
Added "d"
Page 13, line 24: "… all corrections **were** turned off …"
Added "were"
Page 13, lines 28: "… 287.20 and 299.14 nm"
Removed "nm"
Page 14, line 7: Leblanc et al., 2016a is missing in the reference section.
Reference added
Page 14, line 18: The authors state that individual AMOLITE ozone profiles get truncated at an altitude where the total ozone uncertainty exceeds 15%. However, in the ozone curtain plots (e.g. Fig. 8a) the random error appears to exceed 15% at times at the upper altitudes. Please clarify.
Added a few sentences.
Page 15, line 1: "… the impact of long range **transport** events, …"
Already addressed

Page 15, line 9: The term 'backscatter ratio' is used for B_{on}/B_{off} and S in section 2.1. The aerosol backscatter ratio plotted in Fig. 9c (and 12a, 14b, 19b, and 21) appears to be $B_{355} = 1 + S_{355}$. This is very confusing. Please clarify in section 2.1 what the different definitions are. Clarified text

Page 15, lines 10-11: "… intrusions **were** observed (and evidence that a third **started** on 13 November)"

Changed the two words

Page 15, lines 25-27: "There is reasonably good agreement between the ground level measurements **and** the DIAL measurements …" Changed text

Page 15, lines 27-28: The authors state that "the lowest few lidar bins can be unreliable" due to changes in the overlap function caused by temperature fluctuations in the trailer. Some of the ozone curtain plot figures (e.g. Fig 8a) and the ozone time series comparison plots with the surface observations (Figs. 15a and 20a) clearly show that. I suggest to blank out and not show these potentially biased O_3 DIAL measurements at the lower altitudes.

Figures changed

Page 15, lines 29-30: "…and the mixing of the lowest water vapor region …". What do the authors mean by that? Please reword.

Removed text

Page 16, lines 3-4: Fig. 11a indicates that the stratospheric intrusion occurred on 11 November, so elevated O_3 during the night on 10 November is likely due to some other process. As the authors allude to later, transport of O_3 from the industrial area is a possibility. But mixing of higher O_3 concentrations from aloft down to the surface due to mechanical mixing associated with wind speed or direction shear need to be considered.

Made note that the aerosol LIDAR shows plume signature

Page 16, line 12: "... where there **are** …" Instead of 'sulphate' I suggest using 'sulfur compounds' to refer to the H_2S, SO_2, and sulfate aerosol measurements.

Changed wording

Page 16, line 18: Add reference: Jaffe and Briggs, 2012 (Jaffe, D and N. Briggs. (2012). Ozone production from wildfires: A critical review. ATMOSPHERIC ENVIRONMENT. 51. 1-10. 10.1016/j.atmosenv.2011.11.063)

Reference added

Page 16, line 27: "**The diurnal cycles of ozone over three days are** shown …"

Added text

Page 17, lines 5-9: Radar RASS wind direction shown in Fig 16 remains SSE when the smoke plume arrives and does not appear to change very much. Omit this figure and text reference to it.

Deleted text and figure

Page 17, line 23: "… approximately **from** 40 to 65 sr" Added from

Page 17, line 13: "… for determining the **aerosol type** …" Deleted "parcel"

Page 17, line 28-29: "A more typical plot …" Omit this sentence. Sentence removed

Page 18, line 1-3: The S ratio profile can clearly change significantly from night to day, even within the same air mass. Omit this statement or word more carefully.

Deleted sentence

Page 18, line 6: "… **shows** several processes …" Changed "has: to "shows"
Page 18, lines 12-16: "There are also time periods **(6-8 September around 1200 UTC)** where these near 0 ozone features appear to reach closer to the ground**,** extending **from 400 to 2000 m.**"
Changed wording
Page 18, line 20, "… on 8 September **are** an artifact …"
Changed "is" to "are"
Page 18, line 21: "… on September 4 range**d** from …"
Added "d"
Page 18, lines 27-28: "The ground level ozone **increased to 70 ppbv** around 18 UTC on 7 September **and dropped to 50 ppbv** around 300 UTC on 8 September, **which was** mostly due …"
Changed text
Page 19, lines 3-4: "… reaches values of up to **35** ppbv"
Changed text
Page 19, lines 13-14: "… slightly smaller (35 to 55 sr) **compared to 31 August**, likely indicative of more aged smoke **(**see the … in Figure 23c**)**."
Changed text
Page 19, line 17: "… average **when** the smoke plumes were present on …"
Changed "during" to "when"
Page 19, lines 20-21: Aerosol backscatter and extinction often vary differently with wavelength and thus have different Angstroem coefficients. The Angstroem coefficient typically refers to aerosol extinction, which can be computed from the extinction profiles for 355 and 532 nm. The lidar ratio S at different wavelengths is not needed. In fact, the Angstroem coefficient computed from the wavelength dependence of the S ratio convolves the wavelength dependencies of aerosol extinction and backscatter.
Yes you are correct – text changed
References
Page 22, line 27: Ortiz-Amezcua reference is not in alphabetical order.
corrected
Figures
Page 25, line 15: "…for (a) 401 UTC on 10 August and (b) 2103 UTC on 16 August.
corrected
Page 25, line 21: "… due to cloud**s or high** daytime background **light**"
Changed text
Page 26, line 12: "… (c) sulphates (d) PM2.5 …"
corrected
Page 26, line 24: "… (c) sulphates (d) PM2.5 …"
corrected
Figure 5: x-axis label middle plots: (AMOLITE – Sonde)/Sonde (%)
Plot redone to change axis labels

Figure 6: x-axis label middle plot: (Lidar – Sonde)/Sonde (%) plot redone to change axis label
Color curtain plots in Figs. 7, 8, 9, 11, 12, 14, 17, 19, 21, 22: Add numbers at major tick marks of the color scales, not only minimum and maximum values.
Plots redone with new color bar
Figure 11: Add (b) added
Figure 12: Add (b), (c), (d) added
Figure 14: Add (a), (b), (c), (d) added
Figure 16: Omit (see above)
Deleted figure
Figure 17: Create separate scales (similar to Fig. 22)
Created separate scales
Figure 19: Add (a), (b), (c), (d) added
Figure 22: Add (a), (b), (c). Also, axis labels and color scale are very fuzzy.
Plots redone
Figure 23: Add (a), (b), (c) added